remote sensing

Article

In-Orbit Measurements and Analysis of Radio Interference in the UHF Amateur Radio Band from the LUME-1 Satellite

Gara Quintana-Diaz [1,*], Torbjörn Ekman [1], José Miguel Lago Agra [2], Diego Hurtado de Mendoza [2], Alberto González Muíño [2] and Fernando Aguado Agelet [1,3]

[1] Department of Electronic Systems, Norwegian University of Science and Technology (NTNU), 7030 Trondheim, Norway; torbjorn.ekman@ntnu.no (T.E.); faguado@uvigo.es (F.A.A.)
[2] Alén Space, 36350 Nigrán, Spain; jose.lago@alen.space (J.M.L.A.); diego.hurtado@alen.space (D.H.d.M.); alberto.gonzalez@alen.space (A.G.M.)
[3] Escola de Enxeñaría de Telecomunicación, AtlanTTic, University of Vigo, 36350 Vigo, Spain
* Correspondence: gara.quintana@ntnu.no

Abstract: Radio interference in the uplink makes communication to satellites in the UHF amateur radio band (430–440 MHz) challenging for any satellite application. Interference measurements and characterisation can improve the robustness and reliability of the communication system design. Most published results focus on average power spectrum measurements and heatmaps. We apply a low complexity estimator on an SDR (Software-Defined Radio) to study the interference's dispersion and temporal variation on-board a small satellite as an alternative. Measuring the Local Mean Envelope (LME) variability with different averaging window lengths enables the estimation of time variability of the interference. The coefficient of variation for the LME indicates how much the signals vary in time and the spread in magnitudes. In this article, theoretical analysis, simulations, and laboratory results were used to validate this measurement method. In-orbit measurements were performed on-board the LUME-1 satellite. Band-limited interference with pulsed temporal behaviour and a high coefficient of variation was detected over North America, Europe, and the Arctic, where space-tracking radars are located. Wide-band pulsed interference with high time variability was also detected over Europe. These measurements show why operators that use a communication system designed for Additive White Gaussian Noise (AWGN) at power levels obtained from heatmaps struggle to command their satellites.

Keywords: amateur radio band; interference statistics; in-orbit measurements; radio interference; SDR (Software-Defined Radio); small satellite; stationarity; time variability; UHF

Citation: Quintana-Diaz, G.; Ekman, T.; Lago Agra, J.M.; Hurtado de Mendoza, D.; González Muíño, A.; Aguado Agelet, F. In-Orbit Measurements and Analysis of Radio Interference in the UHF Amateur Radio Band from the LUME-1 Satellite. *Remote Sens.* **2021**, *13*, 3252. https://doi.org/10.3390/rs13163252

Academic Editor: Akram Al-Hourani

Received: 29 June 2021
Accepted: 12 August 2021
Published: 17 August 2021

1. Introduction

Communication with satellites is required to operate any spacecraft and offer the service planned, no matter what type of service (telecommunication, Internet of Things (IoT), remote sensing, etc.). The choice of communication parameters should be based on the communication channel properties and the actual interference and noise environment [1]. For Radiofrequency (RF) communication, the radio environment can be measured on-board satellites and provide information to improve the design of the communication system and increase the data throughput. In-orbit spectrum monitoring is paramount for satellite communication systems and has been supported by the European Space Agency (ESA) [2]. Spectrum monitoring is especially important for IoT-over-Satellite networks and for small satellite communication, where uplink interference levels will rise due to the increasing number of IoT devices deployments [3] and small satellites launched [4]. Actual in-orbit interference measurements can complement existing system models for IoT-over-Satellite systems [3,5–7] to improve their real performance and help to design interference mitigation techniques. Spectrum monitoring can help to solve some of the challenges of future satellite systems, such as efficient spectral usage and interference mitigation capabilities [8].

The UHF amateur radio band (430–440 MHz) is a popular frequency band for Telemetry, Tracking and Command (TT&C) of small satellites [9]. Several operators of small satellites have experienced poor uplink performance in this band and have performed interference measurements to analyse the problem [10–13]. In 2014, the University of Vigo carried out a set of preliminary measurements with the HumSat-D satellite, where pulsed interference was detected [10]. In the same year, the University of Würzburg registered high interference levels over central Europe in certain frequencies within the UHF amateur radio band (430–440 MHz) with the UWE-3 satellite [11]. Additional measurements were performed by the University of Vigo using the SERPENS satellite in 2015 and 2016. Strong, consistent uplink interference was detected over North America, Europe, the north of Africa, and the Middle East. Low levels were measured over South America and some regions of Africa [12].

Moreover, Technische Universität Berlin (TU Berlin) has worked on spectrum monitoring in the same band (in addition to VHF, L-band, and S-band) and detected high power interference over North America and Europe using a Software-Defined Radio (SDR) on the International Space Station (ISS) in 2018 [13]. In 2020, TU Berlin launched the SALSAT, a CubeSat to continue their spectrum monitoring activities without the ISS constraints [14], but no results have been published yet. There are also companies, such as Hawk Eye 360 and Aurora Insight, that have started to monitor the spectrum in the last years and are building a constellation to provide frequency spectrum data services, such as geolocation of interference sources [15–17].

Most of the published results focus on the average interference power over a certain measurement duration [10,11,13], omitting the time structure of the interference. In addition, the sub-satellite points of some measurements are limited between -51.6° and $+51.6^\circ$ latitude, specifically, the measurements performed by TU Berlin from the ISS [13] and the SERPENS measurements [18]. Satellite orbits with higher inclination can extend sub-satellite points further north as in Reference [10,11,19]. Heatmaps have been the traditional way of showing the average power of interference [11,13], but they do not show the variability.

The temporal characteristics of the noise/interference impact what type of error correction coding is needed. For example, turbo-codes have a good performance in the presence of Additive White Gaussian Noise (AWGN), but they are weak codes for burst-noise channels [1]. Reed-Solomon error correction coding performs better in burst-noise channels than in AWGN [1]. Channel interleavers can be used in combination with error correction codes for burst noise. A window covering the full temporal dynamics of the interference can be used for the interleaver length since the burst length will be shorter. Moreover, if the interference has a specific time structure, such as pulsed signals, windows of opportunity could be estimated to transmit in between pulses.

To understand the current issues experienced in the TT&C links to small satellites using the UHF radio amateur band, new measurements that combine time and frequency information are needed. Furthermore, the time variability characteristics of the interference can be exploited to improve the communication system design in the band. Ideally, a continuous spectrogram and the probability density function of the interference should be measured to obtain accurate frequency and temporal dynamics. Due to the limited downlink rate of small satellites using the UHF amateur radio band (430–440 MHz) and their power constraints, a low complexity algorithm is desired to measure time and frequency characteristics.

The UHF amateur radio band (430–440 MHz) is shared with other radiocommunication services, such as radiolocation and Earth Exploration Satellites [20]. As a part of the radiolocation service, there are different types of ground radars (type A, B, and C) in the 420–450 MHz band that transmit up to 5 MW of power [21]. Radar type A is used for space object tracking and could be the source of interference of satellite communication in the amateur radio band. In Reference [13], a strong pulsed interference was identified as the ground radar operating in the United Kingdom (UK). Measurements from the SERPENS satellite [12] also suggest that these ground radars can be interfering in the satellite uplink since high power interference was detected over scarcely populated areas.

These type A radars transmit pulse frequency modulation in the form of linear chirps. For the search mode (when surveying space objects), the chirps have a bandwidth of 100–350 kHz, while, for tracking, the bandwidth is 1 or 5 MHz [21]. The pulse width can be 0.25, 0.5, 1, 2, 4, 8, or 16 ms, the average duty cycle is 25%, and the pulse repetition frequency is up to 41 Hz [21]. In Reference [22], the characteristics of the Precision Acquisition Vehicle Entry (PAVE) Phased Array Warning System (PAWS) early warning radars in the United States (US) are described for an environmental impact statement. These radars are located in Cape Cod (Massachusetts), Beale (California), and Clear (Alaska). For these radars, the pulse width for tracking mode can be 0.25, 0.5, 1, 2, 4, 8, and 16 ms, and, for surveillance, 0.3, 5, and 8 ms. The pulse repetition rate can be between 18 and 72 pulses per second. The 3 dB antenna beamwidth is 2.2°, the same as in Reference [21]. The PAVE PAWS radars also transmit high power (around 0.5 MW peak power), so they are an expected source of interference in space.

In this article, we present measurements of the radio environment in the 435 MHz band for satellites in Low Earth Orbit (LEO) using the LUME-1 satellite in the spring of 2021 to support interference characterisation. This satellite has an approximately 98° inclination orbit allowing measurements over the polar areas. The LUME-1 is a CubeSat with limited on-board data processing capabilities and low data rates for communication. This called for the development of simple on-board estimation procedures to obtain the time-frequency interference statistics with low downlink data rate requirements. We performed spectrum measurements over five seconds and estimated the time variability of the interference over windows between 0.21 ms and 27.3 ms, measuring the first-order stationarity by estimating the variance of the Local Mean Envelope (LME) with different lengths of averaging windows.

The contributions of this article can be summarised as: (1) development of a low complexity algorithm to measure time-frequency behaviour of interference to be used in low data rate links, (2) validation of the method through theoretical analysis, simulations, hardware-in-the-loop testing and in-orbit measurements on-board a small satellite, and (3) analysis of the in-orbit interference environment measured in the UHF radio amateur band.

The structure of the paper is as follows. In Section 2, the LUME-1 satellite and its constraints are introduced. The software architecture and measurement algorithm are explained in Section 3, followed by the description of the setup for simulations, laboratory (flatsat), and satellite measurements in Section 4. The theoretical, simulation, lab, and in-orbit measurement results are presented in Section 5 and discussed in Section 6. Finally, conclusions are presented in Section 7.

2. LUME-1 Satellite

LUME-1 was launched on 27 December 2018 from Vostochny in Russia into a 510 km Sun-synchronous orbit. This 2U Cubesat was part of the European project Fire RS, where the University of Porto (Portugal), The Laboratory for Analysis and Architecture of Systems (France), the University of Vigo (Spain), and Alén Space (Spain) collaborated together [23]. The mission ended in June 2019, but the satellite is still operational and available for other research. LUME-1 has a TOTEM SDR on-board [23], allowing the upload of new software with new functionality.

The Norwegian University of Science and Technology (NTNU) collaborates with the University of Vigo and Alén Space to develop and perform new communication experiments with the satellite. The objective is to estimate the in-band radio interference environment in the UHF radio amateur band (430–440 MHz). New software to estimate the time-frequency characteristics of this radio interference was developed at NTNU during

2020. This software was designed considering the constraints of the LUME-1 satellite. The main limitation is the data throughput and communication window. The default gross data rate configuration is 4.8 kbps, extendable to 9.6 kbps, over the UHF amateur radio band at 437.060 MHz, but the obtained net data rate is significantly lower. When using the 4.8 kbps configuration, given the few daily passes over the Vigo ground station due to latitude (42°) and the high level of interference experienced in the uplink, a continuous 1 kbps downlink rate for 5 min per day is a realistic estimate. For the uplink, the communication is degraded, and the estimated actual data throughput is 200 bps for 5 min per day.

In addition, the satellite is tumbling (at approximately 1 rpm), since the Attitude Control and Determination System (ACDS) is planned to be activated at a later stage. The UHF antenna used is the ANT430 antenna from GomSpace, whose antenna pattern is not completely omnidirectional. According to the total gain measured on the GOMX-1 satellite [24] (a 2U CubeSat), the gain can vary between -1.5 to 1.6 dBi, depending on the pointing. The antenna is circularly polarised only when seen from the top (left-hand) and bottom (right-hand). Additional losses can be experienced when pointing differently.

The measurements were planned so that operations were as simple as possible. The TOTEM SDR on-board can have a maximum duty cycle of 50% due to power budget limitations. The RF front-end can be tuned within the 435–438 MHz band, and the dynamic range is approximately 66 dB. The RF bandwidth can be adjusted between 200–56,000 kHz [25], and the ideal sample frequency can be configured within 521–56,000 kSps. In order to use sample frequencies higher than 2 MSps, some digital signal processing must be ported to the Field-Programmable Gate Array (FPGA), requiring extra development. The interference measurement software was developed using GNURadio libraries in C++ and shell scripting.

If the Automatic Gain Control (AGC) was activated, the gain of the Analogue to Digital Converter (ADC) would adapt to the dynamic range of the signal. As the gain cannot be read in real-time, the AGC was deactivated, resulting in a fixed gain for the measurements in this article. Thus, strong signals may saturate the ADC, and weak signals may be below the resolution threshold.

3. Software Architecture and Measurement Algorithm

3.1. Software Architecture

The software consists of two different parts: a shell script controlling the measurements, and a C++ program using GNURadio libraries. The first script starts the measurements with the correct parameters and is responsible for the timing of measurements and file storage. The second programme performs the measurements.

3.2. Measurement Algorithm

The goal of the algorithm is to measure the time-frequency characteristics of the interference received by the LUME-1 satellite. The window of first-order stationarity of the interference is the shortest time window long enough to include a sufficiently varied selection of samples to form a local mean close to the mean envelope in that region. For the stationarity window length, the LME has a low coefficient of variation, and it indicates the length over which an interleaver has to spread information to obtain average interference behaviour.

The In-Phase Quadrature (IQ) samples $x[l]$ are acquired from the ADC at an sample frequency f_s. A Discrete Fourier Transform (DFT) with M frequencies is calculated every M samples of $x[l]$, forming the time frequency representation $X_k[n]$ of the signal. The frequency bin is $k \in \{0, 1, \ldots, M-1\}$, and the time index n denotes that the DFT is applied to $\{x[nM], x[nM+1], \ldots, x[(n+1)M-1]\}$. To estimate the time variability, the magnitude of the DFT, $z_k[n] = |X_k[n]|$, is used [26].

The LME statistics are estimated for each frequency bin. For simplicity, $z_k[n]$ is defined as the time series of the values of the magnitude of the DFT for a particular frequency bin k and $n \in \{0, 1, \ldots, T-1\}$, with T being the total number of DFTs in a single measurement.

The first moment of a distribution is the mean m_1. In the discrete domain, the mean of series $z_k[n]$ with T samples is calculated as the time average

$$m_{1k} = \frac{1}{T} \sum_{n=0}^{T-1} z_k[n]. \tag{1}$$

The second moment (m_2) can be seen as the average power of the signal. This can be calculated as

$$m_{2k} = \frac{1}{T} \sum_{n=0}^{T-1} z_k^2[n]. \tag{2}$$

In order to measure the stationarity of the signals in the traditional way, it would be necessary to acquire all IQ samples and process them on the ground. However, the downlink data throughput is limited, as described in Section 2, so an on-board processing method was developed to reduce the data to be downloaded.

A simple method to measure stationarity that generates little data is to compare local statistics using different time windows. In this article, we analyse the first-order stationarity by measuring the variability of the local mean of the envelope (LME) for different time windows. Short-time windows generally create highly variable local means for stochastic signals. For longer windows, the variability decreases and approaches the mean of the region. If the signal is non-stationary in the region where the data is collected, then no window size smaller than the entire data set gives a LME with small variability. The shortest length where the LME has converged to the regional mean with sufficiently low variance is considered the window of stationarity (first-order). This window length covers the temporal dynamics of the signal. The measures calculated for different time windows are, thus, the first moment m_1, and its variability is calculated using the second moment m_2. Due to software implementation constraints (block coding in GNURadio) and the limitation in the data throughput, the maximum number of windows is fixed to eight in the implemented estimator. Each of the eight time windows ($T_1, T_2, \cdots, T_8$), has a corresponding time series of local means $m_{1k}^{T_i}[l]$ and local second-order moments $m_{2k}^{T_i}[l]$. Figure 1 depicts the hierarchy of $m_{1k}^{T_i}[l]$. The index l indicates the block we consider, where $l \in \{0, 1, \ldots, T/T_i - 1\}$. Equation (3) shows how to calculate the values.

$$m_{1k}^{T_i}[l] = \frac{1}{T_i} \sum_{n=0}^{T_i-1} |z_k[n + l \cdot T_i]|. \tag{3}$$

Doubling the window length in each step $T_{i+1} = 2T_i$ and using square averaging windows allows for a very efficient implementation of the algorithm.

To analyse the variability of $m_{1k}^{T_i}[l]$, the second moment is used. There is a $m_{2k}^{T_i}$ for each time window calculated as

$$m_{2k}^{T_i} = \frac{1}{T/T_i} \sum_{l=0}^{T/T_i-1} \mid m_{1k}^{T_i}[l] \mid^2 . \tag{4}$$

Substituting $m_{1k}^{T_i}[l]$ in Equation (3), we have:

$$\mid m_1^{T_i}[l] \mid^2 = \left| \frac{1}{T_i} \sum_{n=0}^{T_i-1} z_k[n + l \cdot T_i] \right|^2 = \frac{1}{T_i^2} \sum_{n=0}^{T_i-1} \sum_{m=0}^{T_i-1} z_k[n + l \cdot T_i] \cdot z_k[m + l \cdot T_i]. \tag{5}$$

In addition, substituting Equation (5) in Equation (4), $m_{2k}^{T_i}$ can be calculated as

$$m_{2k}^{T_i} = \frac{1}{T/T_i} \sum_{l=0}^{T/T_i-1} \frac{1}{T_i^2} \sum_{n=0}^{T_i-1} \sum_{m=0}^{T_i-1} z_k[n + l \cdot T_i] \cdot z_k[m + l \cdot T_i]. \tag{6}$$

The values of $m_{2k}^{T_i}$ for different T_i depend on the specific signal analysed (see Appendix A). The algorithm implemented provides: (1) an overall mean m_{1k}, (2) overall average power m_{2k}, and (3) measurements of variability of the local mean for different time windows $m_{2k}^{T_i}$.

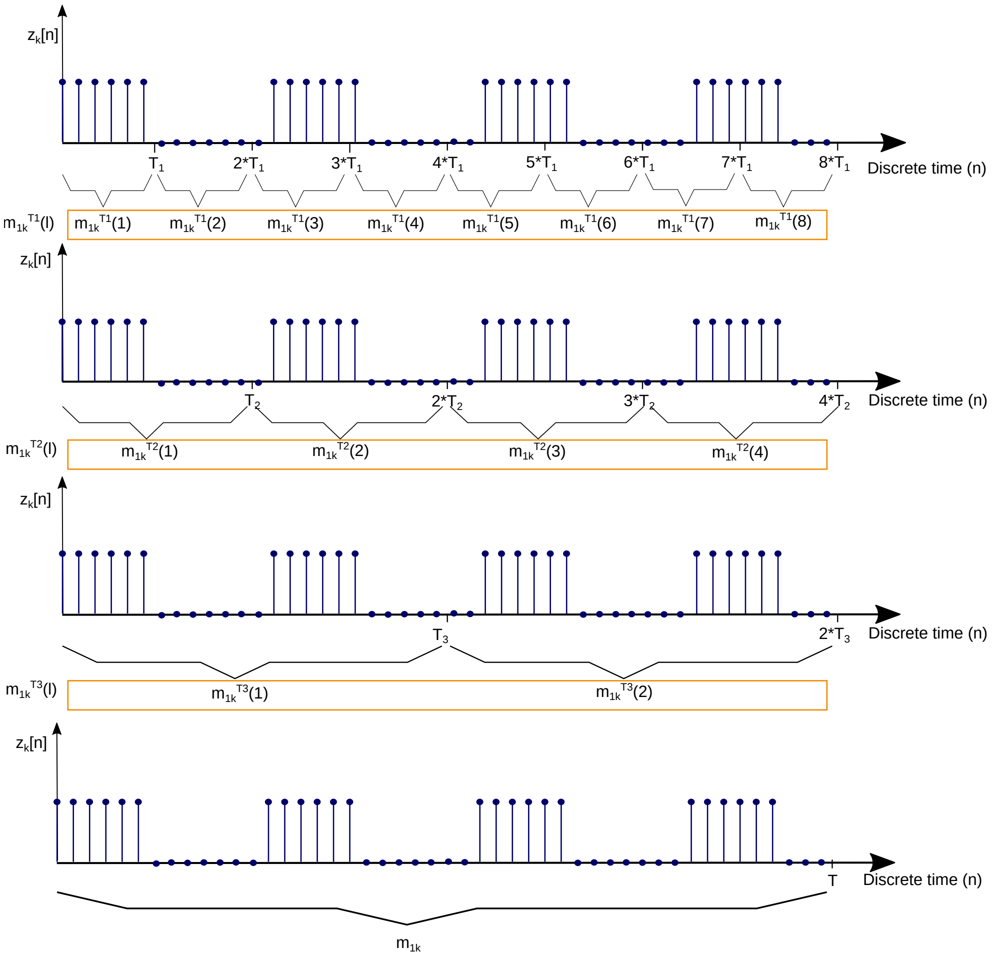

Figure 1. Calculation of the local means $m_{1k}^{T_i}$ and the overall (m_{1k}).

3.3. Coefficient of Variation

The coefficient of variation (CV) is a standardised measure of dispersion defined by the ratio of the standard deviation and the mean. The CV for the envelope for frequency bin k is

$$c_k = \frac{\sqrt{m_{2k} - (m_{1k})^2}}{m_{1k}}. \tag{7}$$

To estimate the window of first-order stationarity, the CV is calculated to analyse the variability of the LME. This standard measure of dispersion is defined as the ratio between the standard deviation of the LME and its mean. Using the output parameters of the algorithm presented, the CV for frequency bin k and time window T_i can be calculated as

$$c_k^{T_i} = \frac{\sqrt{m_{2k}^{T_i} - (m_{1k})^2}}{m_{1k}}. \tag{8}$$

For sufficiently long windows (large T), the coefficient of variation c_k^T converges to zero as $m_{2k}^T \to (m_{1k})^2$. The CV is here used to find the required window length to obtain a local mean sufficiently close to the true mean of the envelope. This window length T_s is considered the window of stationarity in this paper. The limit of convergence is set at

-10 dB; thus, if $(c^{T_s})^2 < 0.1$, then each T_s long local average is considered long enough to include a sufficiently varied selection of samples to form a consistent mean.

For a constant envelope signal, $c = 0$. Then, each observed sample is a good representation of the mean. For independent samples (white noise), the coefficient of variation for a window of length T is obtained in Equation (9) by inserting the second-order moment m_{2k}^T from Equation (A10) into Equation (8).

$$c_k^T = \frac{\sqrt{\left((m_{1k})^2 + \frac{m_{2k} - (m_{1k})^2}{T}\right) - (m_{1k})^2}}{m_{1k}} = \frac{1}{\sqrt{T}} \cdot \frac{\sqrt{m_{2k} - (m_{1k})^2}}{m_{1k}} = \frac{c_k}{\sqrt{T}}. \tag{9}$$

For a complex AWGN, the envelope is Rayleigh distributed and the relationship between the moments, $m_1 = \sqrt{\frac{\pi}{4} m_2}$, renders a coefficient of variation of

$$c_k = \frac{\sqrt{m_{2k} \cdot \left(1 - \frac{\pi}{4}\right)}}{\sqrt{m_{2k} \cdot \frac{\pi}{4}}} = \sqrt{\frac{4}{\pi} - 1} \approx 0.52. \tag{10}$$

Hence, for AWGN, an average window of just three samples is sufficient to obtain a CV below -10 dB, and only 27 samples to obtain it below -20 dB.

4. Measurement Setup

In this section, the setup for the simulations, hardware-in-the-loop (flatsat), and satellite measurements is explained, including the configuration of the measurement software.

One measurement is defined as one C++ programme execution, and a *measurement set* contains a group of measurements. Each measurement has a *duration* and generates a file with date and time as filename. The measurements within a set have a periodicity (time between the start time of two consecutive measurements).

The configuration of the measurements is presented in Table 1. The center frequency was chosen based on the lowest frequency in the UHF amateur radio band measured in Reference [11,13]. In addition, the frequency 435 MHz is in the middle of the ground radar band 420–450 MHz. To reduce software computational power, the sampling frequency was 600 kSps, rounding up the minimum value (521 kSps). To satisfy the Nyquist criterion and avoid aliasing, the RF bandwidth shall be, at least, half of the sampling frequency [26]. The bandwidth setting was chosen to be 200 kHz so that there is a margin with regard to Nyquist; the sampling frequency is then three times the bandwidth.

Table 1. Configuration parameters for simulations, as well as flatsat and in-orbit measurements.

Parameters	**Values**
RF centre frequency (MHz)	435.00
RF bandwidth (kHz)	200.00
Sampling frequency (kSps)	600
Duration (s)	5
Period between measurements (s)	60
Frequency bins	128
Time windows (ms)	0.21, 0.43, 0.85, 1.71, 3.41, 6.83, 13.6, and 27.3
Number of outputs	10
Number of bits	32

The measurement duration should be long enough to find stationarity, but short enough not to measure the spatial variability due to the satellite's movement. The duration was five seconds as a trade-off. This interval corresponds to a movement of a 0.3° angle from nadir (center of Earth). The time between measurements is one minute, which defines the spatial resolution. To resolve the 3° beamwidth (rounding up) used by type A space-tracking radars, a corresponding spatial sampling is performed. Thus, measurements were one minute apart.

There is no maximum bandwidth for the 435 MHz according to the International Amateur Radio Union (IARU) band plan [27], but the Norwegian band plan recommends between 12–20 kHz [28]. Therefore, the frequency resolution should be higher than these values and traded-off against the data size to downlink since the number of frequency bins is proportional to the data size. The number used was 128 to obtain a frequency resolution better than 5 kHz. The resolution for time variability is determined by the first time window, chosen to be 0.21 ms, since it is lower than the shortest pulse width of the radars mentioned in Section 1. The smallest step between windows, which is 2, was chosen for this first round of measurement campaigns. The maximum number of outputs and number of bits was configured to obtain better temporal variation resolution and reduce bit quantisation errors.

To verify the implementation of the proposed estimator, it was first tested on a set of simulated signals describing different possible interference scenarios using the same configuration. The same scenarios were then tested on the TOTEM SDR in the flatsat setup, generating the signals with another SDR to verify the hardware.

4.1. Simulation Setup

The algorithm was developed and tested using an iterative approach. Simulations were the first step to verify the software implementation of the measurement algorithm. The simulations were developed in C++ using GNURadio libraries. The setup consists of a transmitter and a receiver implemented in software. The transmitter sends simulated interference (test signals) and the receiver runs the measurement algorithm.

The test signals used to validate the algorithm were based on the interference environment that can be encountered by a satellite in LEO using the UHF band (430–440 MHz). The four types of signals that were used in testing and validation are: *AWGN*, *Continuous Wave (CW)*, *pulse wave*, and a *chirp* signal. When there are many independent random processes, an AWGN model can be used. A CW is a stationary signal; thus, it can be used to measure full stationarity. Pulsed signals and chirps are chosen because radiolocation is a primary service in the 420–450 MHz band and are expected to be found.

4.2. Flatsat Setup

The next step for verification and validation was to include target hardware in the loop. The main components of the flatsat setup were two SDRs: the Ettus USRP-2901 SDR and the TOTEM SDR. The USRP was used as a transmitter of the test signals. The transmitter software was run on GNURadio companion which is controlled by a desktop computer remotely via Secure SHell (SSH). The version of the TOTEM SDR used in the lab is an upgraded version of the SDR in LUME-1. It was used as the receiver, and it ran the measurement software. The TOTEM SDR encompasses a Xilinx Zynq 7020 System on Chip (SoC) running an embedded Linux system [29], allowing remote access via SSH. The measurement results are saved in files and copied to a computer for analysis.

The lab setup is shown in Figure 2. The USRP is connected to Computer #1 through USB and the SMA transmitter port of the SDR is connected to a 30 dB attenuator to avoid damaging the receiver with strong signals. The output of the attenuator is connected to a 3 dB power splitter. One output of the splitter is connected to the RF port of TOTEM, and the other to a spectrum analyser (Rohde & Schwarz FSV). The power supply provides 5 V to the TOTEM. Computer #2 controls TOTEM and Computer #1 remotely.

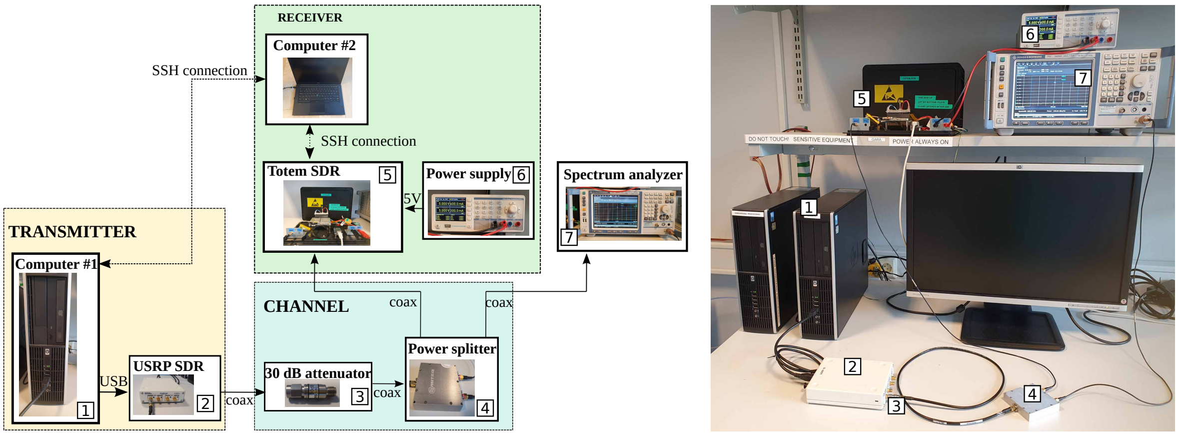

Figure 2. Flatsat setup. The USRP is used as the transmitter for test signals, and the TOTEM SDR (Software-Defined Radio) is the receiver.

The same test signals used in simulations are transmitted by the USRP, properly upconverted to the frequency range which this TOTEM is designed for (430–440 MHz), mixing them with a Local Oscillator (LO). To avoid the effect produced by the LO leakage, the signals (except the chirp) are transmitted with an offset (100 kHz) with respect to the centre frequency, configured in the USRP. The chirp is not shifted 100 kHz because it would be outside the 3 dB bandwidth.

4.3. Satellite Setup

In this article, we present the first measurement results using the algorithm described on-board the LUME-1 satellite. The measurement areas were decided based on where interference has previously been reported in the UHF amateur radio band (America, Europe, north of Africa, and the Middle East) [11–13]; over areas where there are known radar sources and can be of interest to Norway (the Arctic) [21]; and areas in the ocean (South Pacific and South Atlantic). All measurements are referred to as interference over populated areas, except for the last category. The latter are named noise measurements over non-populated areas because the spectra measured had lower power and because there are lower population concentrations.

The Concept of Operations (CONOPS) for the measurement campaigns is as follows:

1. **Plan schedule**. The date and time of passes where the satellite is over the areas of interest are estimated using the Python library *pyorbital* and the corresponding Two-Line Element (TLE) from Celestrak [30].
2. **Upload schedule**. When there is availability over the ground station, the schedule for the measurements is uploaded to the satellite. The schedule includes the date and time to execute the command to run the measurement software, the command, and its parameters.
3. **Run measurement**. TOTEM is turned on and the measurement software runs for five seconds every minute for 10 min. Afterwards, TOTEM is turned off until the next measurement set.
4. **Downlink data**. After all measurements are carried out, the UHF transmitter is turned on to downlink the measurement files.

The size of each data file depends on the number of frequency bins (M), the number of bits per sample (n_b), and the number of outputs of the software (n_u): $M \cdot n_b \cdot n_u$.

In Table 2, the data budget for the measurement algorithm described in this paper, with the configuration of Section 4, is compared to raw spectrum monitoring with the same parameters for five seconds and for one minute continuously. By raw spectrum monitoring, we refer to a spectrogram (commonly known as waterfall plot), which is a representation of the power spectrum of a signal as it changes in time. The on-board processing software provides a data reduction of 203,400 times compared to the 10 min waterfall and 1920 times compared to the five-second waterfall.

Table 2. Data budget to show how the on-board processing software dramatically reduces the data size to be downlinked compared to standard waterfalls.

	(A) Our Software	**(B) 10 min Waterfall**	**(C) 5 s Waterfall**
Sampling frequency (kSps)	600	600	600
Number of frequency bins	128	128	128
Freq. resolution (kHz/bin)	4.7	4.7	4.7
Number of bits	32	32	32
Number of parameters	10	-	-
kBytes per measurement	51.2	11,520,000	96,000
MBytes per measurement	**0.05**	11,520	96

Assuming an available downlink rate of 1 kbps, the time estimated to downlink one set of 10 measurements is shown in Table 3. The number of days to downlink is estimated assuming an average of one pass per day with average five minutes for the 4.8 kbps configuration.

Table 3. Downlink time for the data output of the on-board processing software compared to standard waterfalls.

	(A) Our Software	**(B) 10 min Waterfall**	**(C) 5 s Waterfall**
Net time (h)	0.11	3200	26.6
Effective days	**1.4**	38,400	320

5. Results

First, the validation of theory, simulations, and flatsat results are presented. Second, the in-orbit results obtained from measurements during the first half of 2021 are presented.

5.1. Validation of Theory, Simulations and Flatsat Results

The test signals described in Section 4.1 are used to validate the measurement algorithm. The results analysed are: *average power* (m_{2k}); the variation of m_{2k} from the smallest time window to the largest normalised, referred to as *normalised LME second moment*; and the difference of m_{2k} between consecutive windows normalised ($m_{2k}^{T_i} - m_{2k}^{T_{i+1}}$), named *bin difference*.

The results obtained when measuring different input signals: AWGN; a CW; a pulsed signal with pulses 5 s long and repetition period of 16.67 ms; and a chirp signal with pulses 5 s long, repetition period of 16.67 ms, and 300 kHz bandwidth are shown in Figures 3–5, respectively. All results are measured with the configuration in Table 1. The average power spectrum (m_{2k}) is plotted for AWGN (Figure 3a), a CW (Figure 3b), a pulsed signal (Figure 3c), and a chirp signal (Figure 3d). The signals generated are the same both for simulations and measurements with the flatsat.

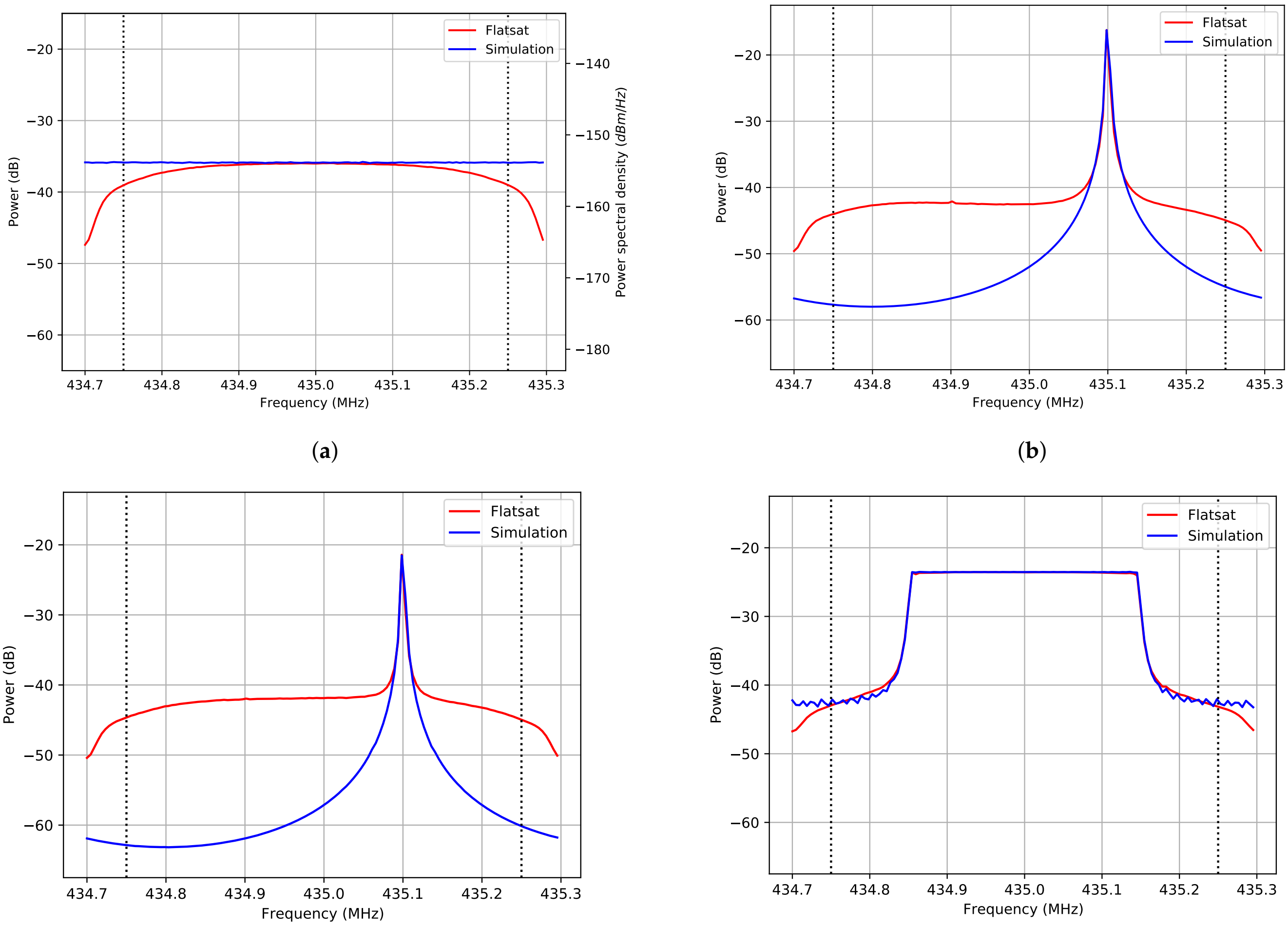

(**a**) (**b**)

(**c**) (**d**)

Figure 3. Test signal comparison of spectrum of average power in simulations (blue curves) and the median of 10 measurements with the flatsat (red curves). Black dotted lines indicate the 3 dB bandwidth of the receive filter. (**a**) AWGN (Additive White Gaussian Noise). (**b**) Complex CW (Continuous Wave) transmitted. (**c**) Complex pulse (5 s long and period 16.67 ms) transmitted. (**d**) Complex chirp (300 kHz wide, 5 s long, and period 16.67 ms) transmitted.

The main differences between the simulation results (blue lines) and the flatsat results (red lines) are the filter, whose frequency response can be seen in Figure 3a, when transmitting AWGN, and the measured noise. In the simulation, the spectrum is flat because the noise transmitted is white (all frequencies are affected in the same way). When the noise is transmitted in the flatsat setup, the spectrum measured is not completely flat because of the receive filter. The filter is configured to have a bandwidth of 200 kHz for the AD9364 transceiver chip. Nevertheless, the measured 3 dB bandwidth is larger (from 434.75 to 435.25 MHz), so this is the band analysed in the remainder of the paper (indicated by vertical black dotted lines). The TOTEM in the lab setup was calibrated for the spectral power density, but, for the TOTEM on LUME-1, there is no power calibration available. Measured power on LUME-1 is a relative measure and is displayed in dB.

In both the CW simulations and flatsat results (Figure 3b), there is one peak at 435.1 MHz. This peak is expected since a complex tone is transmitted at 100 kHz and modulated onto the 435 MHz carrier. In the pulsed case (Figure 3c), there is one peak at around 435.1 MHz since the transmitted signal was also shifted 100 kHz from the centre frequency. For a 5 s long pulse, the sidelobes appear at multiples of 0.2 kHz, but there is not enough frequency resolution (4.7 kHz) to distinguish them. The spectrum of a chirp signal with 300 kHz bandwidth can be seen in Figure 3d. The chirp was directly modulated onto the RF carrier at 435 MHz, without shifting it 100 kHz, so that it could fit in the 3 dB bandwidth of the receiver.

To detect at which time window a signal becomes stationary, the time statistics of the moments can be analysed. In Figure 4, the normalised LME second moment, for different signals, is shown. It compares theoretical results (blue dashed lines), simulation results for all frequency bins (blue circles), and flatsat results (all frequency bins in black asterisks, and the bin with the highest power with a red cross). It shows that the time variability of the local averages decreases when the window size increases. In the AWGN case (Figure 4a), the normalised second moment for LME decreases following the result in Equation (A13) and converges to $\pi/4$ after some time for all frequency bins. For the CW (Figure 4b), the values are stable and do not change significantly with the time windows since a CW is a stationary signal at all time scales for the bin with the carrier, which is the bin with the highest power. The rest of the bins are the sidelobes of the signal. The lower the sidelobes, the lower signal to noise ratio, and the signal approaches the properties of an AWGN.

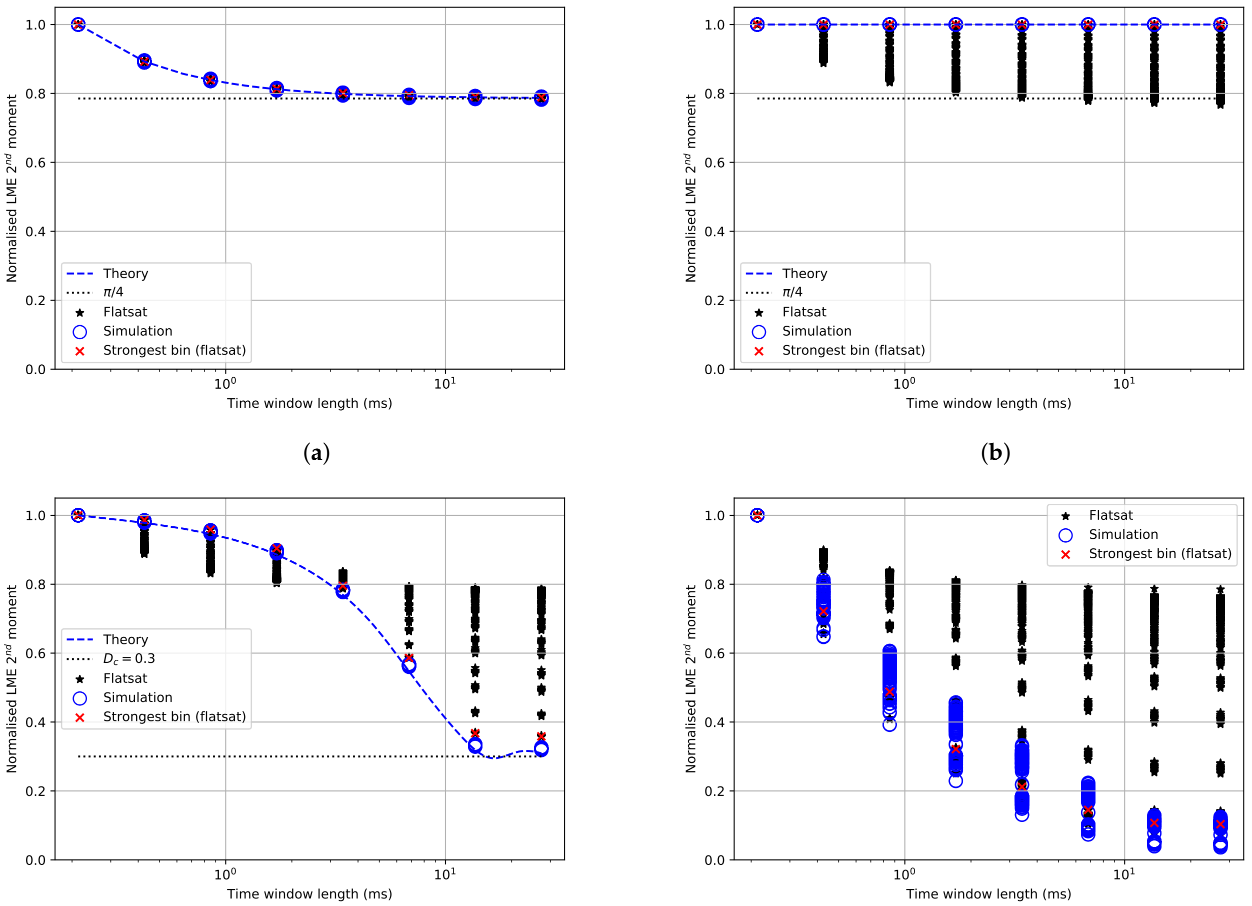

(**a**) (**b**)

(**c**) (**d**)

Figure 4. Comparison of the normalised LME second moment in theory, simulations and measurements with the flatsat. The pulse and the chirp signal have a pulse length of 5 s and a period of 16.67 ms. (**a**) Normalised Local Mean Estimator (LME) second moment for AWGN. (**b**) Normalised LME second moment for a CW. (**c**) Normalised LME second moment for a complex pulse. (**d**) Normalised LME second moment for a complex chirp.

The pulsed signal curve (Figure 4c) changes the behaviour considerably, depending on whether the time window is smaller than the pulse length (T_p) and/or the pulse repetition period (T_r). When the time window is larger than the pulse repetition period, the curve flattens out. The last two data points in the curve correspond to 13.6 ms and 27.3 ms, and, since the curve is converging, it indicates that the pulse repetition period is in that range. The indication in the graph is validated since the pulse repetition period is 16.67 ms. To be able to obtain a better estimation of the period, more time windows would be needed.

In Figure 5, the difference between the values of consecutive windows normalised is shown. For the AWGN, the curve has a decreasing exponential trend, and, for the CW, the values are zero for the highest frequency bin. There should not be any variation between time windows for a continuous signal. In the case of the pulsed signal, the peak is in between the fifth ($T_5 = 3.4$ ms) and sixth point ($T_6 = 6.8$ ms). Since the pulse transmitted was 5 s long, the curve is as expected. Furthermore, all theoretical, simulation, and flatsat values in Figure 5 are similar, validating the algorithm.

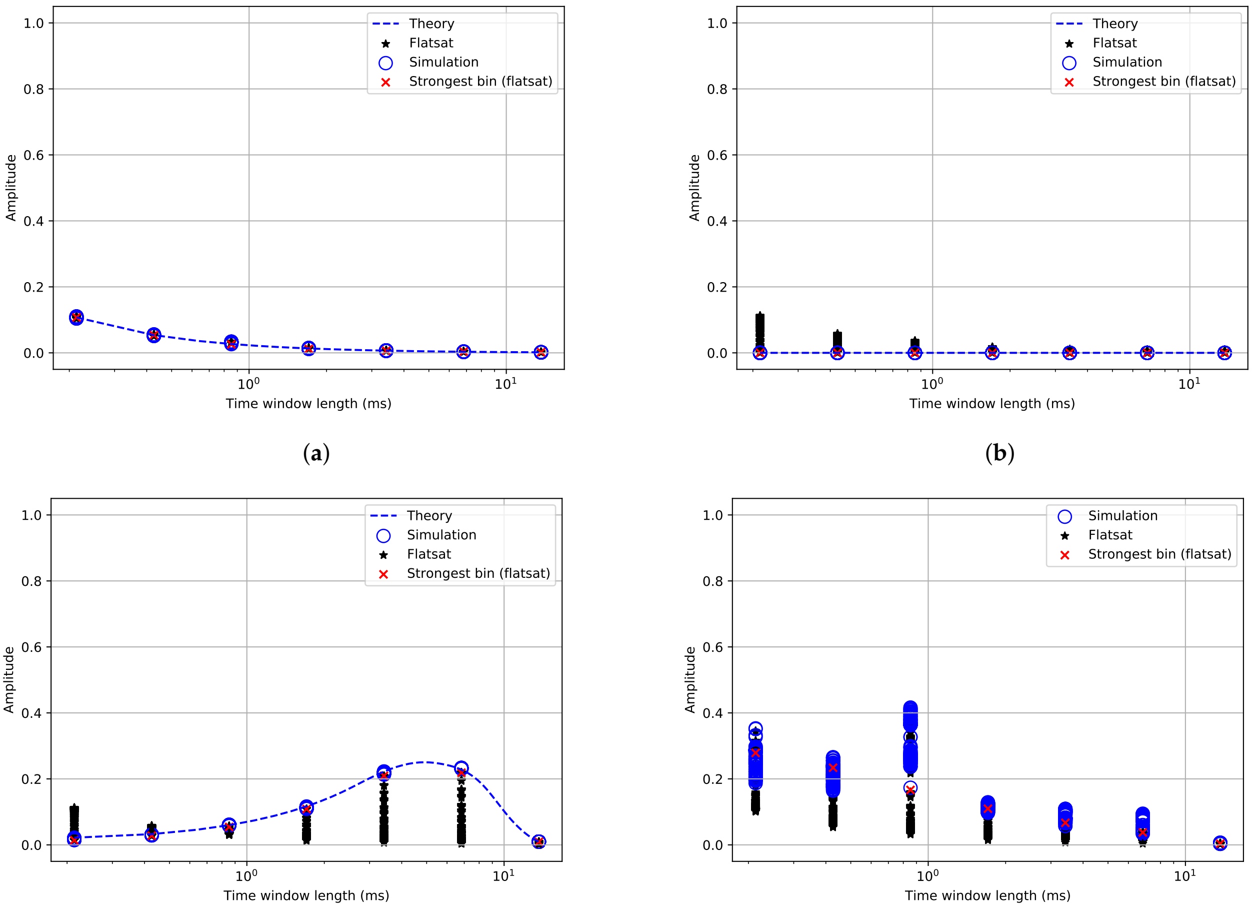

(**a**) (**b**)

(**c**) (**d**)

Figure 5. Comparison of bin difference in theory, simulations and measurements with the flatsat. The pulse and the chirp signal have a pulse length of 5 s and a period of 16.67 ms. (**a**) AWGN bin difference. (**b**) CW bin difference. (**c**) Complex pulse bin difference. (**d**) Complex chirp bin difference.

5.2. In-Orbit Results

The first in-orbit measurement was performed in December 2020. Three more measurement campaigns were carried out in the first half of 2021 during the months of February, May, and June. Each measurement set consisted of 10 individual calls to the measurement software as previously explained. In total, 300 individual measurements were executed. The main areas that the measurements covered were the South Pacific, South Atlantic, North America, Europe, and the Arctic.

5.2.1. Measurements over Non-Populated Areas

To analyse in-orbit interference measurements, it is important to measure over non-populated areas to estimate the noise floor. Since absolute power levels cannot be obtained from the satellite, these measurements can be used as a lower bound for the power. The estimation of the in-orbit noise floor can be compared to the AWGN measurements with the flatsat setup to verify that the spectrum shape is as expected.

The measurements over non-populated areas were taken over the South Pacific and South Atlantic, as shown in Figure 6a. In total, 60 measurements were performed in this area, but five of them contained CW interference (red circles in the map). Thus, they were grouped with the measurements over populated areas since they were obtained close to the South American coast.

The average power spectrum (m_{2k}) was estimated over five seconds for each of the measurements. In Figure 6b, the 90% percentile, median, and 10% percentile of the average power for each bin of all average power spectra are shown. The shape of the spectrum is very similar to the result obtained in the lab (Figure 3a). In the bandwidth of interest (434.8–435.2 MHz), the median value of all measurements and all frequency bins is -41 dB. The 10% percentile is -44 dB, and the 90% percentile is -39 dB, including all frequency bins. In Figure 6c, the coefficient of variation c_k was calculated using Equation (7) and compared to the theoretical value of AWGN in Equation (10), which is approximately 0.52. The CV for noise in-orbit measurement is similar to that of the AWGN but slightly higher for the median and the 90% percentile.

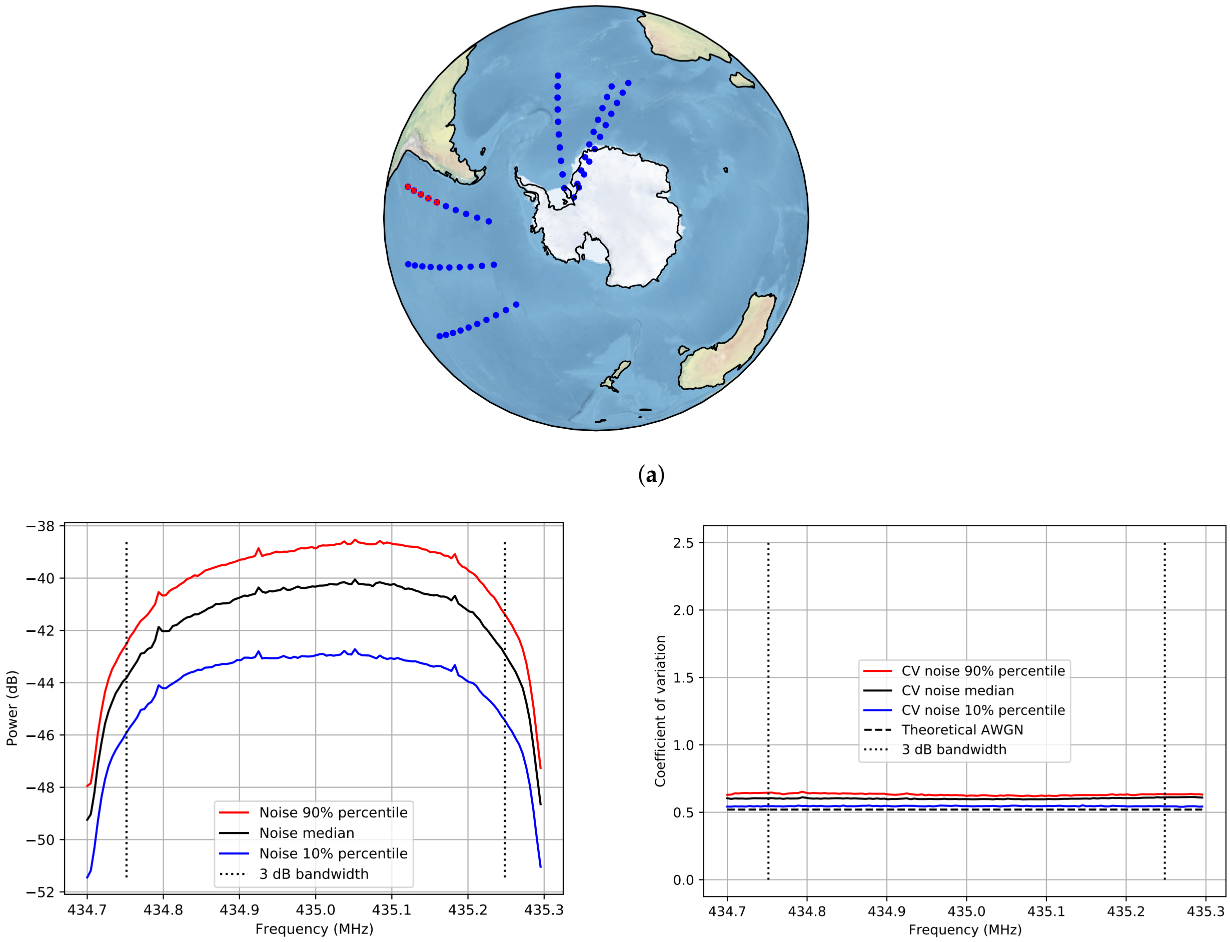

(**a**)

(**b**) (**c**)

Figure 6. Time-frequency behaviour of measurements over non-populated areas. (**a**) Sub-satellite points for measurements over non-populated areas (blue circles) and close to populated areas (red circles). (**b**) Spectrum of average power (m_{2k}). (**c**) Coefficient of variation (CV). A high coefficient indicates high spread in the measured envelope.

The variability of the LME as a function of averaging window length was also measured (Figure 7). All measurements have similar temporal behaviour, so a representative example of the normalised LME second moment for all the frequencies is presented in Figure 7a. The normalised LME second moment follows the AWGN time behaviour converging to approximately $\pi/4$. This trend can also be seen in Figure 7b, where the normalised LME second moment was plotted for all frequency bins of all noise floor measurements (blue circles). The blue dashed line represents the theoretical trend for the AWGN, the red crosses show the highest bin measured in the flatsat setup, and the dotted line $\pi/4$. The in-orbit results show a slightly higher deviation from the flatsat results for AWGN for longer windows.

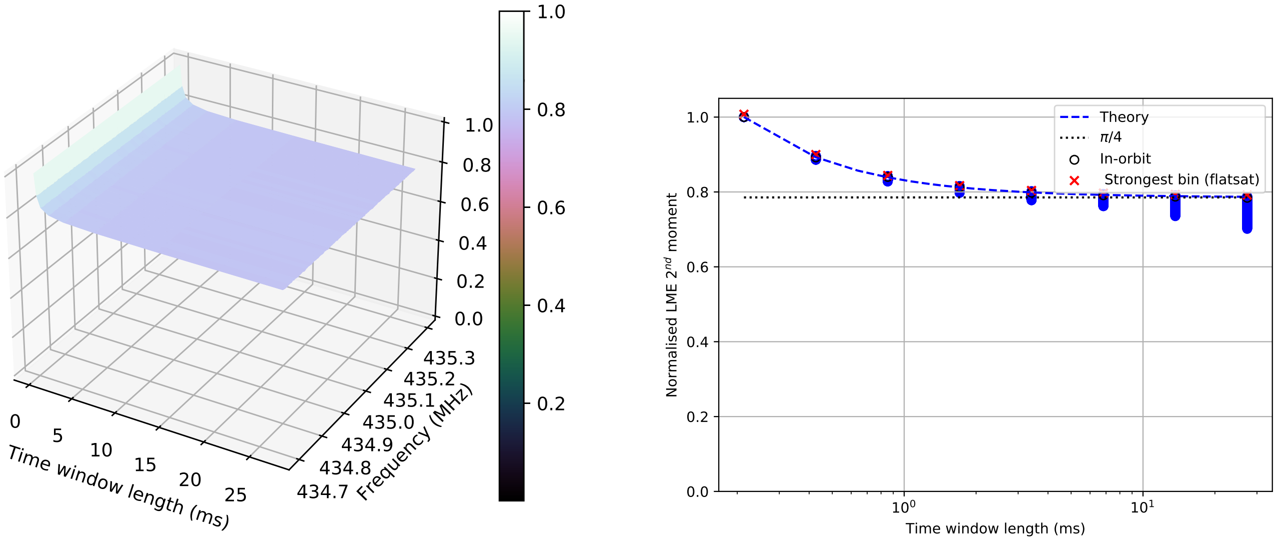

(**a**) (**b**)

Figure 7. Time behaviour of measurements over non-populated areas. (**a**) Normalised LME second moment for different time windows in 3D. (**b**) Normalised LME second moment for different time windows in 2D.

5.2.2. Measurements over Populated Areas

The measurements performed close to populated areas are shown in Figure 8a, and they are referred to as interference measurements hereafter. The 90% (red line) and 10% percentile (blue line) and the median (black continuous line) of all average power spectra measured over populated areas are compared to the median of the noise measurements over non-populated areas (black dashed line) plotted in Figure 8b. The 10% percentile signal spectrum has about the same power level as the noise median spectrum.

A band-limited signal of around 300 kHz of low power can be observed in the 10% percentile signal spectrum, but it is more visible in the signal median and the 90% percentile spectrum as it has higher power. Since the band-limited signals appear clearly in the signal median, they are present at least in half of the measurements. Furthermore, the 90% percentile spectrum has around 7 dB higher power than the median in the centre frequency and there seems to be a wide-band signal in addition to the band-limited signal.

The dispersion of the spectra can be analysed using the CV in Figure 8c. The 10% percentile is close to the median of the CV for noise measurements. The CV for the signal median and the signal 90% percentile have a different tendency to that of the noise measurements. The CV in these cases is higher, which means the dispersion is higher and the probability for communication to be hit by interference significantly larger than the average power is higher than for AWGN. In the CV for the median, we observe that the increase of the dispersion is band-limited, as seen in the average power spectrum (Figure 8b), while, for the 90% percentile, the band-limited signal is combined with other wide-band signals with even higher dispersion.

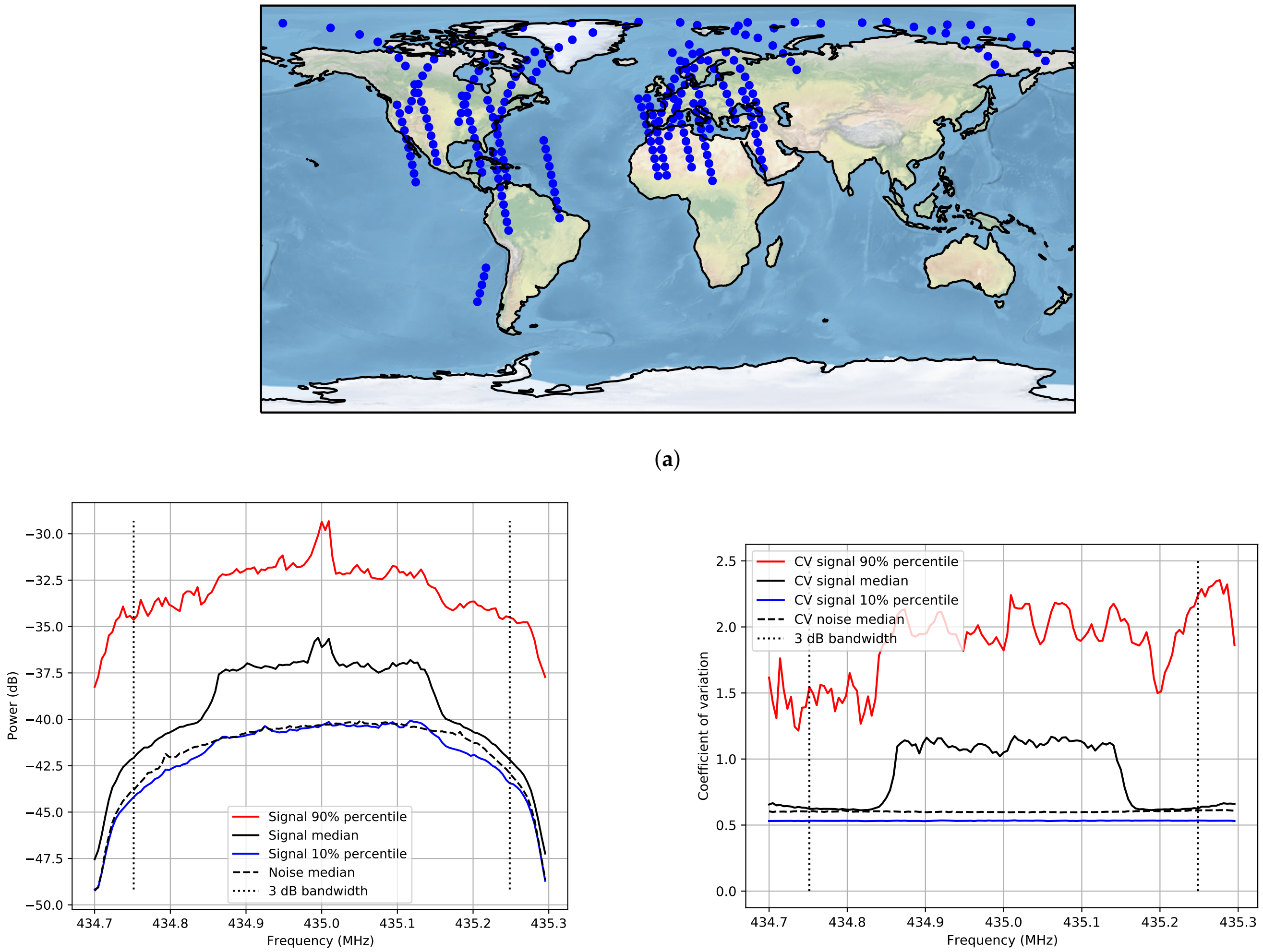

(**a**)

(**b**) (**c**)

Figure 8. Time-frequency behaviour of measurements over populated areas. (**a**) Sub-satellite points for measurements over populated areas. (**b**) Spectrum of average power (m_{2k}). (**c**) CV. A high CV indicates high spread in the measured envelope.

The Empirical Cumulative Density Function (ECDF) of the measured interference power of all frequency bins shows the probability of getting hit by an interference no larger than a certain power. The ECDF for the interference is estimated for three regions $R1$–$R3$ covering West and East Europe and northern Africa, together with the Middle East (Figure 9). In the map shown in Figure 9a, the northern parts of the plot are between 35° and 70° (marked with crosses in the map and with dashed lines in the plot), and the southern part is between 0° and 35° (circles in the map and a blue continuous line in the plot). Each of the northern regions represents 35° of longitude, while the southern region represents 70° of longitude. The points in the map represent the sub-satellite points where the satellite measured received power. The power of all frequency bins within the 3 dB bandwidth is included to estimate the ECDFs (Figure 9b). As a reference, the red curve is the distribution of all regions.

There is a clear difference between the interference experienced in the regions in the north ($R1$ and $R2$) and south ($R3$). The region $R3$ is affected in less than 20% of the points by signals with a power higher than −38 dB. The power increases about 7 dB for regions $R1$ and and 6 dB in $R2$ for 20% of the points in relation to region $R3$. In general, the sub-satellite points with lower latitude experience less interference because they were acquired over less populated areas. Nevertheless, their distribution is different from the noise distribution (dotted black line).

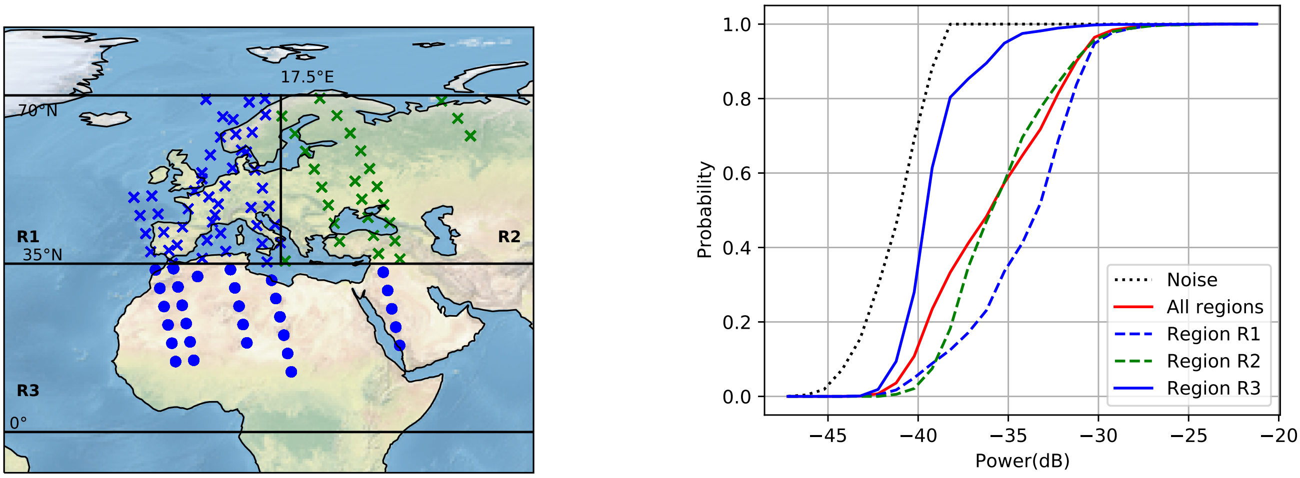

(**a**) (**b**)

Figure 9. Power distribution over Europe, northern Africa, and the Middle East. (**a**) Measurement locations over several orbits. The northern regions cover 35° of longitude and latitude; and the southern region, 70° of longitude and 35° of latitude. (**b**) Empirical Cumulative Density Function (ECDF) of received power over the three regions and all frequency bins within the 3 dB bandwidth, including the noise floor measurements (black dotted line). The blue continuous line is linked to the blue circles in the map and dashed lines to crosses. Red line is the ECDF of all the points in the map.

Figure 10 shows the results of the same procedure applied to the measurements carried out over America, redefining the areas of interest. The coastal regions (*R*4, *R*6 and *R*7) cover 40° of longitude, while the middle region (*R*5) covers 30°. The latitude limits are 0°, 35°, and 70°, as shown in the map. The interference levels are lower than in Figure 9b. The regions that are more affected by the interference are *R*4 and *R*6. Around 20% of the points in these regions experience an interference level higher than −36 dB. Furthermore, two different behaviours can be observed in region *R*6: 57% of the points experience interference levels above −38 dB, while the rest of the points follow a different trend with lower power. The regions *R*5 and *R*7 follow a distribution that is not so different from the noise (dotted black line).

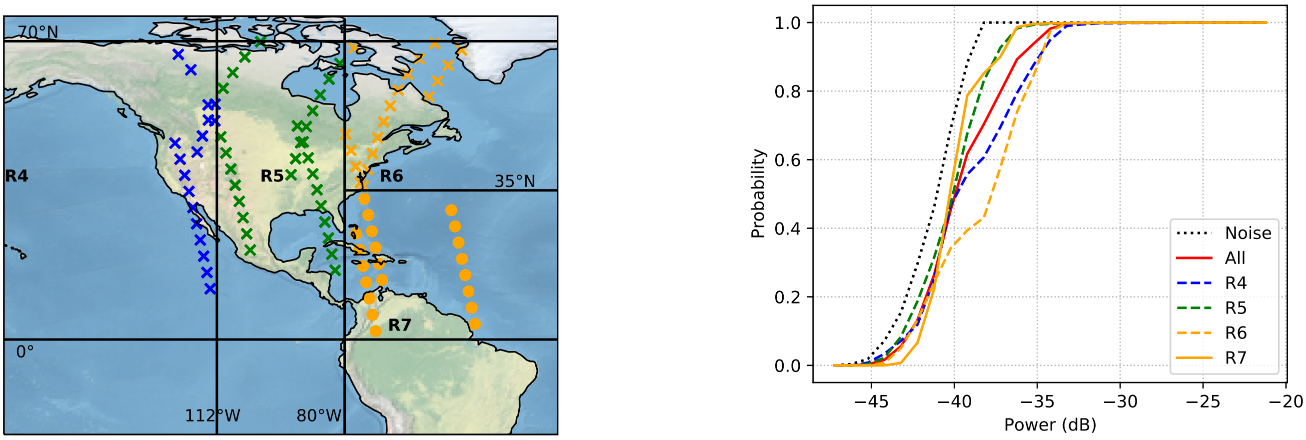

(**a**) (**b**)

Figure 10. Power distribution over America divided in four regions. The colour blue is for western, green for central, and orange for eastern areas. (**a**) Measurement locations over several orbits. The regions *R*4, *R*6 and *R*7 cover 40° of longitude; and the middle region *R*5 covers 30°. *R*4 and *R*5 cover 70° of latitude; and *R*6 and *R*7, 35°. (**b**) ECDF of received power over the four regions, including the noise floor measurements (black dotted line). The yellow continuous line is linked to the circles in the map and dashed lines to crosses. The red line is the ECDF of all the points in the map.

One representative example of a measurement where the band-limited signal can be seen in the average power spectrum is shown in Figure 11a, obtained close to Greenland. Two types of interference signals can be distinguished: one narrow-band at 434.74 MHz and the band-limited signal with a bandwidth around 300 kHz, which is about 7 dB higher than the rest of the spectrum. At the same time, the CV indicates that the band-limited signal has a higher spread as CV increases up to 2.6. The temporal behaviour of the frequency bins differs (Figure 11b,c). When analysing both figures, we can see the main behaviour of the band-limited signal converging to about 0.25. The edges of the spectrum are a combination of noise and the sidelobes of the band-limited signal and converge to around 0.6.

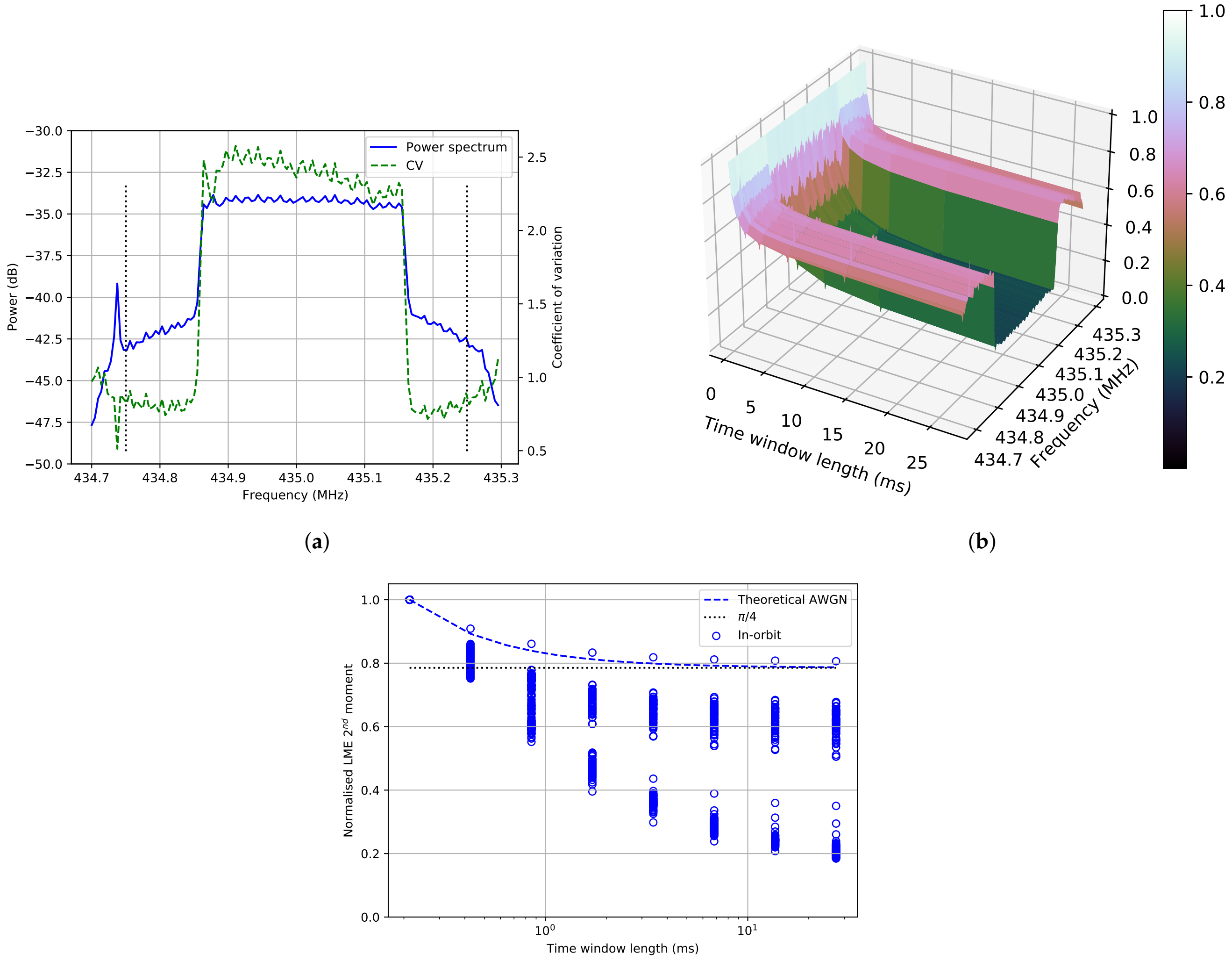

(**a**) (**b**)

(**c**)

Figure 11. Example of a five second measurement with different types of signals over Greenland. (**a**) Average power spectrum (m_{2k}) and coefficient of variation. If there was no time variability in the mean, it would be zero. (**b**) Normalised LME second moment for different time windows for all frequency bins in 3D. (**c**) Normalised LME second moment for different time windows for all frequency bins.

5.2.3. Window of Stationarity

To analyse the first-order stationarity of the interference measurements, the window of stationarity is estimated at the −10 dB level for the CV (see Section 3). The measurements have been divided into four regions (Figure 12a): South Pacific and South Atlantic (named the Antarctic), America, the Arctic, and Europe. In this section, when we refer to Europe, we include the north of Africa and the Middle East. The estimation of the window of stationarity over the frequencies has been divided into two parts: the frequencies that are within the band-limited interference (434.83–435.19 MHz); and the ones outside but within the 3 dB bandwidth (434.75–434.83 MHz and 435.19–435.25 MHz).

In Figure 12b, the window of stationarity for frequencies outside the band-limited signal is shown. Most measurements have a window of stationarity below 6.83 ms, particularly the Antarctic measurements. The only regions that have stationarity windows longer than 27.31 ms are Europe and the Arctic.

In Figure 12c, the frequency bins analysed are the ones within the band-limited interference. For the Antarctic measurements, there is no big change. For the rest of the regions, the window of stationarity increases for more measurements. About 29% of the Arctic measurements have a window of stationarity longer than 27.3 ms. For America and Europe, it is around 9% and 31%, respectively. There is a considerable difference for measurements over America between Figure 12b,c, since the largest window of stationarity in Figure 12b is 6.83 ms, and, in Figure 12c, it is longer than 27.3 ms.

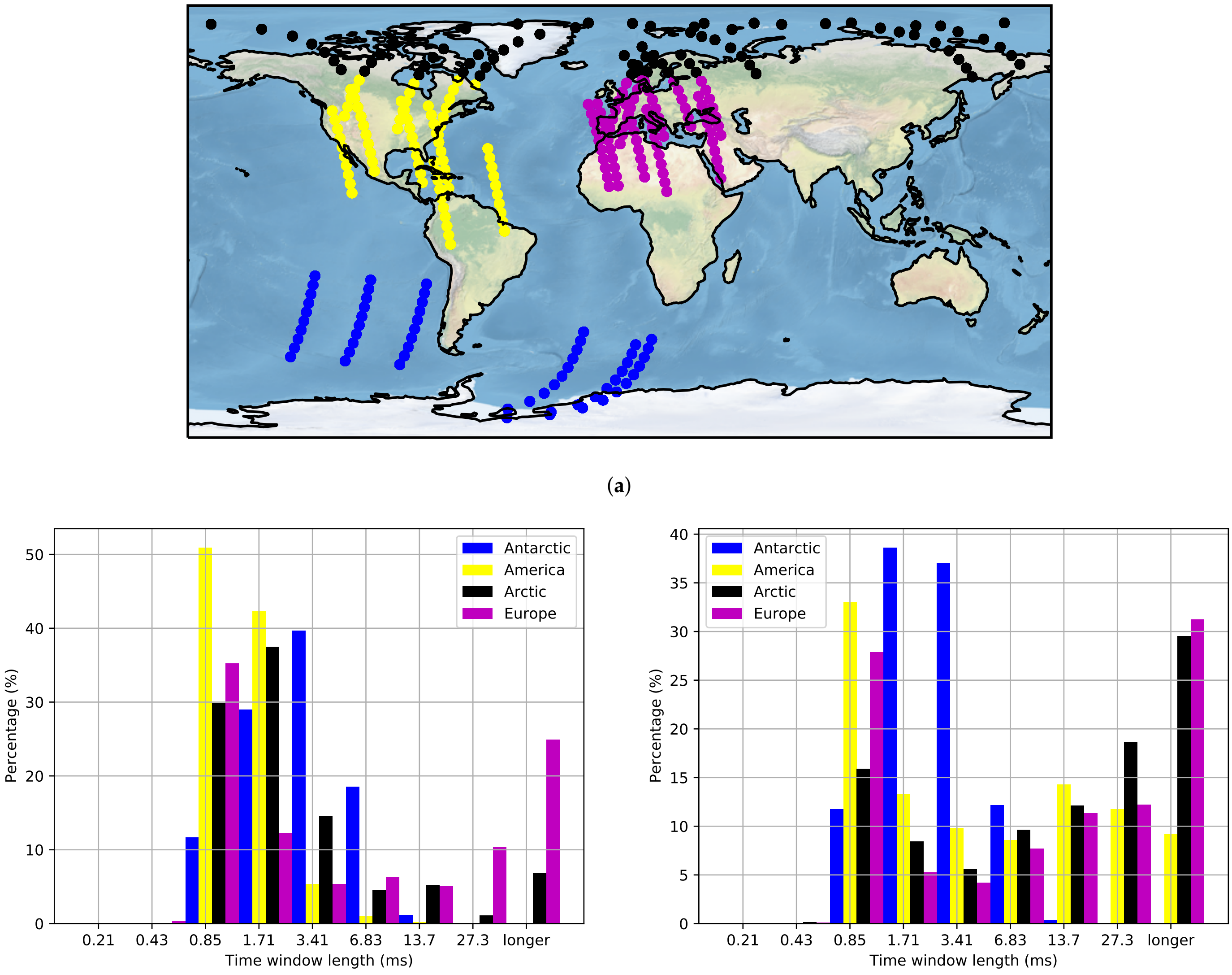

(**a**)

(**b**) (**c**)

Figure 12. Window of stationarity results of in-orbit measurements. (**a**) Measurement locations grouped into four categories: Antarctic (blue), America (yellow), Arctic (black), and Europe (magenta). (**b**) Histogram of stationarity window per region (outside band-limited interference bandwidth). (**c**) Histogram of stationarity window per region (within band-limited interference bandwidth).

5.2.4. Interference with Time Structure

In the measurements performed, interference with time structure was observed in different areas. Figure 13a shows the sub-satellite points where different types of interference were detected visually. There are two types of interference with time structure: band-limited (red crosses) and wide-band (black circles). Interference with no time structure is marked with blue stars, and the position of the type A ground radars in the 420–450 MHz band, according to Reference [21], is marked with black triangles and numbers.

The band-limited interference was observed where the radars are present, and the bandwidth is consistent with the chirp bandwidth of these radars for the search mode (100–350 kHz for radar type A [21]). The bandwidth of the interference was estimated automatically based on two different parameters: the average power spectrum (m_{2k}) and the ratio of moments, $(m_{1k})^2/m_{2k}$. Both show similar results as depicted in Figure 13b. Where the algorithm did not detect a signal, the bandwidth was set to zero. It can be seen that the m_{2k} approach has slightly lower performance when the interference has low power compared to the noise. In these cases, the estimation of the bandwidth has a better performance when using the ratio of moments approach. Figure 13c shows the CV of the envelope for the cases where band-limited interference was visually detected. It was estimated by calculating the median of c_k over the bandwidth where the band-limited interference was detected. The cases where the ratio is zero are due to the same reason as before, i.e., where the bandwidth was not detected automatically, the CV was set to zero. The CV gives an indication of the spread and dispersion of the envelope. For AWGN, the CV is 0.52 since the spread in envelope is low. In Figure 13c, the CV is higher than the AWGN and up to 2.6. This means that the dispersion of the envelope is higher, and the probability of getting hit by stronger than average interference is higher than if it was an AWGN with the same average power.

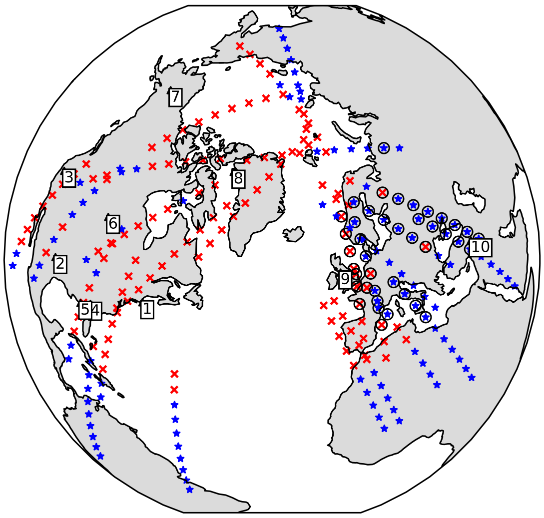

(**a**)

Figure 13. *Cont.*

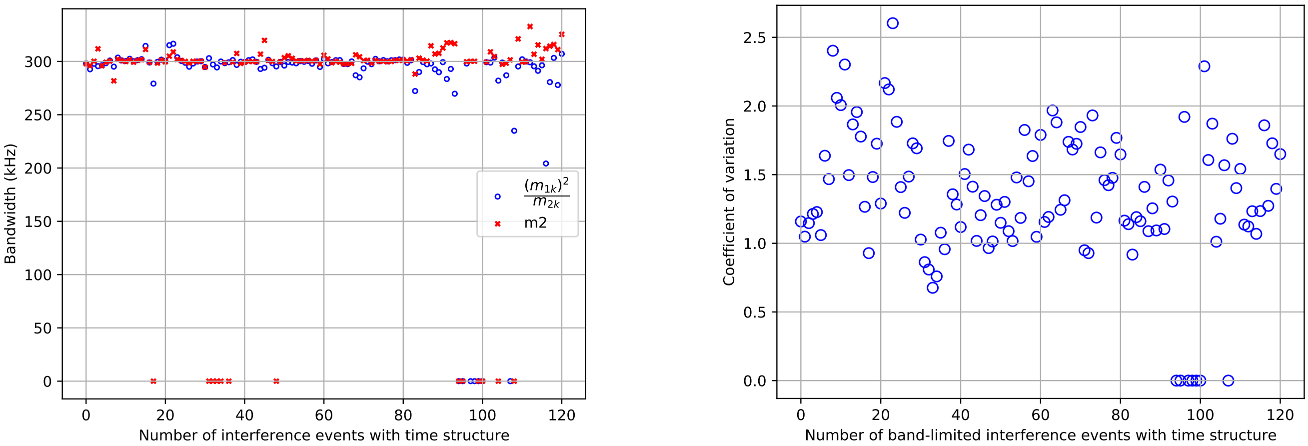

(**b**) (**c**)

Figure 13. Detection of band-limited interference, estimation of bandwidth, and CV. (**a**) Measurement location where band-limited interference (red crosses) and wide-band interference (black circles) with time structure was detected by visual analysis, rest of locations (blue stars), ground radar locations (black triangles with numbers) [21,31]. 1: Massachusetts (U.S.), 2: Texas (U.S.), 3: California (U.S.), 4: Georgia (U.S.), 5: Florida (U.S.), 6: North Dakota (U.S.), 7: Alaska (U.S.), 8: Thule (Greenland), 9: Fylingdales Moore (United Kingdom), 10: Pirinclik (Turkey). (**b**) Automatic bandwidth estimation using two parameters: the ratio of moments, $(m_{1k})^2/m_{2k}$; and the average power spectrum (m_{2k}). The cases with zero bandwidth corresponds to when the automatic detection failed. (**c**) The median of the CV over the bandwidth of the automatically detected band-limited interference. The cases with zero correspond to when the automatic detection failed. A high coefficient indicates high spread in the measured envelope.

6. Discussion

The interference measured over non-populated areas has similar behaviour to the AWGN behaviour both in frequency and time. The in-orbit spectrum measured (Figure 6b) shows the frequency response of the system that was measured in the lab (Figure 3a). The measurements over non-populated areas can be used as an in-orbit relative noise floor and justify the use of heatmaps over these areas since the behaviour is close to Gaussian. In the power spectrum, there is a variation that can be caused by the tumbling of the satellite that introduces a variation in antenna gain and polarisation, as well as a variation in internal temperature. On several of the measurement tracks, the satellite moved from daylight (highest internal temperature) to eclipse (lowest internal temperature). This could also be the explanation why the temporal behaviour is not completely Gaussian; perhaps there is a slow variation of internal temperature causing this difference.

For the populated areas, the power levels of the interference are higher than the noise floor. In these areas, there can be a lot of interference sources, such as ground stations for different satellites and amateur radio activity. The results show that the measured interference over different regions has different frequency and time behaviour. There are different types of interference: some have AWGN statistics, others show CW temporal behaviour, and the last type has a pulsed tendency (both band-limited and wide-band). The AWGN is predominant on the edges of the frequency response where no other signals are present. The narrow-band signals (CW) can be beacons from radio amateurs and would be possible to locate with more measurements.

The interference that has roughly 300 kHz bandwidth has higher power than the noise floor and different statistics than CW and AWGN. This signal requires a longer time window to obtain a consistent estimate of the average envelope than the AWGN. It is consistently present over the areas where there are known type A radars. The frequency band measured in this paper is 435 MHz and is exactly in the middle of the band for ground radars (420–450 MHz), so it is expected to see some of that behaviour. The bandwidth also matches the chirp bandwidth for the search mode of type A radars used for space-tracking (100–350 kHz) [21].

There was also another type of interference with time structure detected over central Europe. However, this interference has a bandwidth higher than what can be seen with the configuration of these measurements (higher than 500 kHz). This interference could be caused by the radar chirps from the tracking mode (1 MHz wide), but it can also be a different source.

The time behaviour measured shows high variability within five seconds. Average power is a useful measure to design a system that works for the average interference environment, but it does not take the temporal structure and dispersion of the interference into account. The CV can be helpful to estimate how much time variability the signal has. The CV is a measure of dispersion. So, if a band has significant power above the general noise floor and the CV is high, the peak power is much higher than the average power. The high CV observed over Europe, the Arctic, and the coastlines of North America indicates a much larger spread in amplitude than for AWGN. A communication system designed to cope with AWGN at the noise levels given by a heatmap fails under these circumstances. The stationarity measurements and the CV show that the interference is not AWGN over populated areas.

The window of stationarity can be used as the required length of an interleaver to obtain average coding performance for each interleaved interval. Even though a lot of measurements are required to increase the reliability of the estimation of the length of this window, we can identify regional trends. For frequencies in the range 434.75–434.83 MHz and 435.19–435.25 MHz, the length could be less than 14 ms for most cases and regions. For the Arctic and Europe, longer lengths are needed for more reliability. In the band 434.83–435.19 MHz, there is a significant portion of measurements over America, Europe, and the Arctic, where window lengths longer than 27 ms are needed.

The results presented are part of the measurement campaigns performed in the first half of 2021. Calibration measurements to estimate absolute power levels are planned for the next phase. A ground station will transmit test signals, such as a CW, with a known power to calibrate the in-orbit power results. Furthermore, global measurements will be performed to obtain an overall view of the interference environment. These measurements will have a lower frequency resolution to decrease the data size of the campaign. The center frequency will also be modified to observe the frequency variability. It is important that future measurements include ECDF measurements of the interference IQ samples, as well as temporal characteristics to enable the choice of the right countermeasures to obtain robust uplink communication.

7. Conclusions

In this article, we have presented an algorithm that can measure frequency and time characteristics of in-orbit interference with low downlink data rate requirements. The method is validated through theoretical analysis, simulations and hardware-in-the-loop testing, and executed in-orbit measurements on the LUME-1 satellite. The studied frequency band was the UHF amateur radio frequencies commonly used for TT&C of small satellites. The in-orbit interference measurements were carried out over the South Pacific, South Atlantic, North America, Europe, North Africa, the Middle East, and the Arctic during the spring of 2021.

As expected, higher interference levels were generally detected over populated areas. Three different time behaviours were distinguished: AWGN, narrow band CW, and pulsed. The pulsed behaviour was seen by analysing the variation of the local mean of the average envelope as a function of window length. High values of the coefficient of variation were estimated in regions with band-limited interference that have significant power over the general noise floor. For that interference, the peak power is much higher than the average power. This interference was observed over areas with known type A ground radars in the UHF band around 435 MHz, and the observed bandwidth of 300 kHz is consistent with the chirp bandwidth for radar search mode [21]. Furthermore, wide-band interference with pulsed behaviour was measured over Europe, but the bandwidth could not be estimated due to the limited bandwidth of 500 kHz in the measurements.

A global measurement campaign is planned to provide a world overview of the interference environment in the selected band. Calibration measurements using a ground station transmitting to the satellite will enable the use of absolute power levels. Furthermore, different centre frequencies will also be studied, and ECDF measurements of the IQ samples will be planned to obtain the proper interference statistics to design the countermeasures required to improve the reliability of the satellite uplink in the UHF amateur radio band.

Author Contributions: Conceptualisation, G.Q.-D., T.E. and F.A.A.; methodology, G.Q.-D. and T.E.; software, G.Q.-D.; validation, G.Q.-D. and D.H.d.M.; formal analysis, G.Q.-D. and T.E.; investigation, G.Q.-D., J.M.L.A., A.G.M. and F.A.A.; resources, F.A.A., A.G.M., D.H.d.M. and J.M.L.A.; data curation, G.Q.-D.; writing—original draft preparation, G.Q.-D.; writing—review and editing, G.Q.-D., T.E., F.A.A., J.M.L.A. and D.H.d.M.; visualisation, G.Q.-D.; supervision, T.E. and F.A.A.; project administration, T.E.; funding acquisition, T.E. and F.A.A. All authors have read and agreed to the published version of the manuscript.

Funding: The work of the Norwegian University of Science and Technology (NTNU) is supported by the Norwegian Research Council (Grant No. 270959), the Norwegian Space Agency, and the Centre of Autonomous Marine Operations and Systems (NTNU AMOS). The work of the University of Vigo has been funded by Programa de Cooperación Transfronteriza INTERREG V-B SUDOE (Fondos FEDER) under the project "Wildfire picosatellite constellation & uavs remote sensing: active fire mapping and management" (Grant No. FIRE-RS, SOE1/P4/E0437) and by Ministerio de Economía y Competitividad— Programa Estatal de Investigación, Desarrollo e Innovación Orientada a los Retos de la Sociedad under the project "Development of a small satellite for spectrum monitoring and validation of robust communications" (Grant No. ESP2016-79184-R).

Institutional Review Board Statement: Not applicable.

Informed Consent Statement: Not applicable.

Data Availability Statement: The data presented in this study are available on request from the corresponding author.

Acknowledgments: Gara Quintana Díaz wishes to acknowledge the help of her colleagues, Roger Birkeland and Jens Abraham, and Nicolás Molina Padrón for useful discussions of ideas and results.

Conflicts of Interest: The authors declare no conflict of interest. The funders had no role in the design of the study, in the collection, analyses, or interpretation of data, in the writing of the manuscript, or in the decision to publish the results.

Appendix A. Properties of Local Mean Envelope of a Stationary Stochastic Process

A discrete-time envelope $z[n]$ is generated by a stationary stochastic process with mean μ_z and variance σ_z^2. The first-order moment is $m_1 = \mathbb{E}\{z[n]\} = \mu_z$, and the second-order moment is $m_2 = \mathbb{E}\{z[n]^2\} = \sigma_z^2 + \mu_z^2$. The length T ($T \in \{0, 1, 2, \ldots\}$) sliding local average of the envelope $z[n]$ can be obtained as

$$u[n] = h[n] * z[n], \tag{A1}$$

where $h[n]$ is the square window Finite Impulse Response (FIR) filter normalized with the length T to get the average,

$$h[n] = \begin{cases} 1/T, & \text{for } n = 1, \ldots, T \\ 0, & \text{else.} \end{cases} \tag{A2}$$

The LME is obtained as $u[n]$ sub-sampled by a factor T. The moments of $u[n]$ are hence the moments for the LME. The first-order moment (mean) of the LME is the mean of $u[n]$, which is μ_z. The second-order moment depends on the length T. To obtain it, we study the correlation function for $u[n]$, the filtered stochastic signal

$$r_u[k] = \mathbb{E}\{u[n] \cdot u[n+k]\} = r_h[k] * r_z[k], \tag{A3}$$

where $r_z[k]$ is the correlation for the envelope $z[n]$, and

$$r_h[k] = h[k] * h[k] = \begin{cases} \dfrac{T-|k|}{T^2}, & \text{for } -T \le k \le T \\ 0, & \text{else.} \end{cases} \tag{A4}$$

As $z[n]$ is real valued and $z[n] \ge 0$ then $r_z[k] = r_z[-k]$ and $r_u[k] \ge 0$. The second-order moment for $u[n]$, denoted m_2^T, is obtained as $r_u[0]$

$$\begin{aligned} m_2^T &= r_u[0] = r_h[k] * r_z[k]|_{k=0} = \sum_{k=-\infty}^{\infty} r_h[k] \cdot r_z[0-k] \\ &= \frac{1}{T}\left\{ r_z[0] + \frac{2}{T}\sum_{k=1}^{T}(T-k) \cdot r_z[k] \right\}. \end{aligned} \tag{A5}$$

For $T = 1$, we obtain $m_2^1 = m_2$, which is the power of the signal. Hence, the LME has the mean $\mu_u = \mu_z = m_1$ and the variance $\sigma_u^2 = m_2^T - (m_1)^2$, where the second-order moment is given in Equation (A5).

By normalising the LME second-order moment by the power of the signal, we obtain the moment ratio as

$$\frac{m_2^T}{m_2} = \frac{1}{T} + \frac{2}{T^2}\sum_{k=1}^{T}(T-k) \cdot \frac{r_z[k]}{r_z[0]}. \tag{A6}$$

The ratio starts at 1 for $T = 1$ and converges to $\dfrac{(m_1)^2}{m_2}$ for large T, as for a sufficiently large T the LME is equal to the mean of the envelope. How fast the ratio converges depends on the correlation function $r_z[k]$. If the correlation function falls off fast, the m_2^T will converge fast. We use the coefficient of variation to evaluate the convergence of the LME.

Appendix A.1. Example Signal: Constant Envelope

A signal with constant envelope $z[n] = a$, as a CW, has a constant envelope correlation $r_z[k] = a^2$. The ratio in Equation (A6) is then $\dfrac{(m_2^T)^2}{m_2} = 1$, for all T.

Appendix A.2. Example Signal: Square Pulse

For a square pulse wave that is on with magnitude a for a duration T_p with a period T_r, the envelope correlation is periodic $r_z[k] = r_z[k - T_r]$. For $T_p < T_r/2$, the correlation is:

$$r_z[k] = \begin{cases} a^2 \cdot \dfrac{T_p - k}{T_p}, & \text{for } |k| < T_p \\ 0, & \text{for } T_p < |k| < T_r - T_p. \end{cases} \tag{A7}$$

The moment ratio, Equation (A6), of a pulse converges to the duty cycle:

$$\lim_{T\to\infty} \frac{m_2^T}{m_2} = \frac{(m_1)^2}{m_2} = \frac{\left(\dfrac{T_p}{T_r} \cdot a\right)^2}{\dfrac{T_p}{T_r} \cdot a^2} = \frac{T_p}{T_r}. \tag{A8}$$

Appendix A.3. Example Signal: White Signal

For a signal with independent but equally distributed samples, the correlation is

$$r_z[k] = \mathbb{E}\{z[n] \cdot z[n+k]\} = \begin{cases} \mathbb{E}\{z^2[n]\} = m_2, & \text{for } k = 0 \\ \mathbb{E}\{z[n] \cdot z[n+k]\} = (m_1)^2 & \text{for } k \neq 0 \end{cases}. \tag{A9}$$

Inserting this correlation into Equation (A5), the second-order moment for the LME for a white signal is obtained as

$$m_2^T = (m_1)^2 + \frac{m_2 - (m_1)^2}{T} = \mu_z^2 + \frac{\sigma_z^2}{T}. \tag{A10}$$

For large T, the second-order moment m_2^T converges to the squared mean of the envelope.

For an AWGN, the samples are zero mean complex normal distributed, and the envelope has a Rayleigh distribution. The $\mathbb{E}\{z^2[n]\} = m_2$ is the power of the signal. The mean of the envelope is

$$m_1 = \mu_z = \mathbb{E}\{z[n]\} = \sqrt{\frac{\pi}{4} \cdot m_2}, \tag{A11}$$

and the variance is

$$\sigma_z^2 = m_2 - \mu_z^2 = m_2 \cdot \left(1 - \frac{\pi}{4}\right). \tag{A12}$$

The normalised second moment given in Equation (A6) is then

$$\frac{m_2^T}{m_2} = \frac{\pi}{4} + \frac{1}{T} \cdot \left(1 - \frac{\pi}{4}\right), \tag{A13}$$

which converges to

$$\lim_{T \to \infty} \frac{m_2^T}{m_2} = \frac{(m_1)^2}{m_2} = \frac{\pi}{4} \tag{A14}$$

for large T.

References

1. CCSDS. TM Synchronization and Channel Coding—Summary of Concept and Rationale. In *CCSDS Green Book*; CCSDS Secretariat, National Aeronautics and Space Administration: Washington, DC, USA, 2012.
2. European Space Agency (ESA). ESA Artes Frequency Monitoring. 2016. Available online: https://artes.esa.int/projects/board-spectrum-monitoring-obsm (accessed on 8 August 2021).
3. Chan, C.C.; Al-Hourani, A.; Choi, J.; Gomez, K.M.; Kandeepan, S. Performance Modeling Framework for IoT-over-Satellite Using Shared Radio Spectrum. *Remote Sens.* **2020**, *12*, 1666. [CrossRef]
4. Kulu, E. Nanosats Database. 2021. Available online: https://www.nanosats.eu/ (accessed on 8 August 2021).
5. Homssi, B.A.; Al-Hourani, A.; Krusevac, Z.; Rowe, W.S.T. Machine Learning Framework for Sensing and Modeling Interference in IoT Frequency Bands. *IEEE Internet Things J.* **2021**, *8*, 4461–4471. [CrossRef]
6. Lin, Z.; Lin, M.; de Cola, T.; Wang, J.B.; Zhu, W.P.; Cheng, J. Supporting IoT With Rate-Splitting Multiple Access in Satellite and Aerial-Integrated Networks. *IEEE Internet Things J.* **2021**, *8*, 11123–11134. [CrossRef]
7. Lin, Z.; Lin, M.; Champagne, B.; Zhu, W.P.; Al-Dhahir, N. Secure and Energy Efficient Transmission for RSMA-Based Cognitive Satellite-Terrestrial Networks. *IEEE Wirel. Commun. Lett.* **2021**, *10*, 251–255. [CrossRef]
8. Jia, M.; Gu, X.; Guo, Q.; Xiang, W.; Zhang, N. Broadband Hybrid Satellite-Terrestrial Communication Systems Based on Cognitive Radio toward 5G. *IEEE Wirel. Commun.* **2016**, *23*, 96–106. [CrossRef]
9. ITU-R: Report ITU-R SA.2312-0. *Characteristics, Definitions and Spectrum Requirements of Nanosatellites and Picosatellites, as Well as Systems Composed of Such Satellites*; ITU: Geneva, Switzerland, 2014.
10. Aguado Agelet, F.; Nodar López, D.; González Muiño, A. Preliminary noise measurements campaign carried out by HUMSAT-D during 2014. In Proceedings of the ITU Conference and Workshop on the Small Satellite Regulation and Communication Systems, Prague, Czech Republic, 2–4 March 2015; pp. 1–21.
11. Busch, S.; Bangert, P.; Dombrovski, S.; Schilling, K. UWE-3, in-orbit performance and lessons learned of a modular and flexible satellite bus for future pico-satellites. *Acta Astronaut.* **2015**, *117*, 73–89. [CrossRef]

12. Quintana-Diaz, G.; Nódar-López, D.; Aguado Agelet, F.; Capelletti, C.; Ekman, T. Detection of radio interference in the UHF amateur radio band with the Serpens satellite. *Adv. Space Res.* **2021**, under review.
13. Buscher, M. *Investigations on the Current and Future Use of Radio Frequency Allocations for Small Satellite Operations*; Universitätsverlag der TU Berlin: Berlin, Germany, 2019; Volume 7 .
14. Großhans, J.; Quan, H.; Balke, A.; Lohse, A.; Maaß, A. SALSAT—An innovative nanosatellite for spectrum analysis based on SDR technology. In Proceedings of the 69th International Astronautical Congress (IAC), Bremen, Germany, 1–5 October 2018; pp. 1–5.
15. HawkEye 360. RFGeo™—HawkEye 360. Available online: https://www.he360.com/products/rfgeo/ (accessed on 1 May 2021).
16. Sarda, K.; Zee, R.E.; CaJacob, D.; Orr, N.G. Making the Invisible Visible: Precision RF-Emitter Geolocation from Space by the HawkEye 360 Pathfinder Mission. In Proceedings of the 32nd Annual AIAA/USU Conference on Small Satellites, Logan, UT, USA, 4–9 August 2018.
17. Aurora Insight Inc.. Aurora Insight. Available online: https://aurorainsight.com/ (accessed on 1 May 2021).
18. Santilli, G.; Vendittozzi, C.; Cappelletti, C.; Battistini, S.; Gessini, P. CubeSat constellations for disaster management in remote areas. *Acta Astronaut.* **2018**, *145*, 11–17. [CrossRef]
19. The SALSAT Mission by TU Berlin: From Berlin into Space. Available online: https://www.tu.berlin/en/research/themenportal-forschen/2020/juli/salsat-mission/ (accessed on 1 May 2021).
20. International Telecommunication Union. *Radio Regulations*; ITU: Geneva, Switzerland, 2008; pp. 47–100.
21. ITU-R: Recommendation ITU-R M.1462-1. *Characteristics of and Protection Criteria for Radars Operating in the Radiolocation Service in the Frequency Range 420–450 MHz*; ITU: Geneva, Switzerland, 2019.
22. United States Air Force. *Pave Paws Early Warning Radar Operation Project Continued Operation of the Solid-State Phased-Array Radar System (SSPARS) Also Known As Pave Phased Array Warning Systems (PAWS) Cape Cod Air Force Station MA*; Technical Report; United States Air Force: Washington, DC, USA, 2009 .
23. Pérez-Lissi, F.; Aguado-Agelet, F.; Vázquez, A.; Yañez, P.; Izquierdo, P.; Lacroix, S.; Bailon-Ruiz, R.; Tasso, J.; Guerra, A.; Costa, M. FIRE-RS: Integrating land sensors, cubesat communications, unmanned aerial vehicles and a situation assessment software for wildland fire characterization and mapping. In Proceedings of the 69th International Astronautical Congress, Bremen, Germany, 1–5 October 2018.
24. GOMspace | NanoCom ANT430. Available online: https://gomspace.com/shop/subsystems/communication-systems/nanocom-ant430.aspx (accessed on 1 June 2021).
25. Alén Space. *TOTEM Motherboard Datasheet*; Alén Space: Vigo, Spain, 2018.
26. Oppenheim, A.V. *Signals & Systems*, 2nd ed.; Prentice-Hall signal Processing Series; Prentice-Hall: Upper Saddle River, NJ, USA, 1997.
27. International Amateur Radio Union (IARU). IARU Region 1 UHF Band Plan. 2020. Available online: https://www.iaru-r1.org/wp-content/uploads/2021/03/UHF-Bandplan.pdf (accessed on 1 June 2021).
28. Norwegian Radio Relay League (NRRL). Norwegian Band Plan 70 cm (432–438 MHz). 2017. Available online: https://www.nrrl.no/images/bandplaner/BP2016-70cm.pdf (accessed on 1 June 2021).
29. Quintana-Díaz, G.; Birkeland, R.; Honoré-Livermore, E.; Ekman, T. An SDR Mission Measuring UHF Signal Propagation and Interference between Small Satellites in LEO and Arctic Sensors. In Proceedings of the 33rd Annual AIAA/USU Conference on Small Satellites, Logan, UT, USA, 3–8 August 2019.
30. CelesTrak. Available online: https://celestrak.com/ (accessed on 1 June 2021).
31. ITU-R: Recommendation ITU-R SA.1260-1. *Feasibility of Sharing between Active Spaceborne Sensors and Other Services in the Range 420–470 MHz*; ITU: Geneva, Switzerland, 2017.